Shear-induced depinning of thin droplets on rough substrates

Ninad V. Mhatre and Satish Kumar[†]
Department of Chemical Engineering and Materials Science, University of Minnesota,
Minneapolis, MN 55455, USA

Abstract

Depinning of liquid droplets on substrates by flow of a surrounding immiscible fluid is central to applications such as crossflow microemulsification, oil recovery, and waste cleanup. Surface roughness, either natural or engineered, can cause droplet pinning, so it is of both fundamental and practical interest to determine the flow strength of the surrounding fluid required for droplet depinning on rough substrates. Here, we develop a lubrication-theory-based model for droplet depinning on a substrate with topographical defects by flow of a surrounding immiscible fluid. The droplet and surrounding fluid are in a rectangular channel, a pressure gradient is imposed to drive flow, and the defects are modeled as Gaussian-shaped bumps. Using a precursor-film/disjoining-pressure approach to capture contact-line motion, a nonlinear evolution equation is derived describing the droplet thickness as a function of distance along the channel and time. Numerical solutions of the evolution equation are used to investigate how the critical pressure gradient for droplet depinning depends on the viscosity ratio, surface wettability, and droplet volume. Simple analytical models are able to account for many of the features observed in the numerical simulations. The influence of defect height is also investigated, and it is found that when the maximum defect slope is larger than the receding contact angle of the droplet, smaller residual droplets are left behind at the defect after the original droplet depins and slides away. The model presented here yields considerably more information than commonly used models based on simple force balances, and provides a framework that can readily be extended to study more complicated situations involving chemical heterogeneity and three-dimensional effects.

[†]Email address for correspondence: kumar030@umn.edu

1 Introduction

Pinning of liquid droplets on topographical or chemical defects on solid surfaces, and depinning by flow of a surrounding immiscible fluid, are central to a diverse range of applications. Crossflow microemulsification involves droplets of a dispersed phase released into a channel through membranes. The droplets can pin on the membrane, and a continuous phase flows through the channel to depin the dispersed-phase droplets and form an emulsion.^{1,2} In oil recovery and oil waste removal, water flow is used to depin oil droplets that are pinned inside rock crevices and contaminated soil.^{3–5} An important class of surface cleaning methods involves applying a fluid flow to depin and remove contaminants present in the form of liquid droplets on solid surfaces.⁶

The importance of droplet depinning on solid surfaces by a surrounding fluid flow has motivated prior experiments aimed at understanding the limiting case of depinning of a single droplet. Some works examine the behavior of an oil droplet in a surrounding water flow,^{7–10} and some investigate the behavior of a water droplet in a surrounding air flow.^{11–13} For each case, the droplet depins and slides on the surface above a critical flow rate of the surrounding fluid.

Some of the works discussed above use simple force-balance models to rationalize experimental observations. In these models, a shear force acting on the droplet due to a surrounding fluid flow drives depinning, and the surface-tension force acting along the droplet contact line resists depinning. Below the critical flow rate of the of the surrounding fluid, the forces are balanced and the droplet remains pinned, and above the critical flow rate, the shear force exceeds the surface-tension force, causing droplet depinning.^{9,10,12}

In these models, the shear force acting on the droplet, F_s , is typically estimated by assuming a static droplet with a spherical-cap shape, a circular contact line, and a Stokes-like drag law.¹⁴ It is found that $F_s \sim (\mu_s v_h R_0^2)/h_{max}$, where μ_s is the surrounding fluid viscosity, h_{max} is the maximum droplet height, v_h is the surrounding fluid velocity at the maximum droplet height, and R_0 is the radius of the circular contact line. The surface-tension force, F_{surf} , is estimated by assuming a static droplet with a circular contact line. It is also assumed that the contact angle in the entire advancing half of the droplet is equal to the advancing contact angle, θ_{acl} , and that the contact angle in the entire receding half of the droplet is equal to the receding contact angle, θ_{rcl} . Under these assumptions, $F_{surf} \sim \sigma D(\cos \theta_{acl} - \cos \theta_{rcl})$, where σ is the

interfacial tension and D is the diameter of the circular contact line.¹² Some force-balance models also calculate the surface-tension force by approximating the contact-line shape as an ellipse^{15–17} or a parallel-sided drop.^{17,18}

Although force-balance models are useful for rationalizing experimental observations, they have several important shortcomings. First, they cannot provide predictions of steady or transient droplet shapes, which is information of fundamental interest. Second, advancing and receding contact angles must be input into these models and are assumed to be constant. However, in practice these angles may be spatially dependent due to natural or engineered surface variations. Third, force-balance models do not explicitly incorporate the influence of surface topography or wettability variations on droplet depinning. While these factors can be implicitly accounted for through the advancing and receding contact angles, it may not always be clear how parameters characterizing surface variations are related to these angles. Explicitly accounting for surface variations is essential for developing mathematical models that can be used to design surfaces with topography and wettability variations for a desired Additionally, force-balance models cannot provide information about the application. mechanics of pinning to and depinning from surface features, which is also information of fundamental interest. Nevertheless, it should be noted that force-balance models combined with experimental data can yield good predictions of the surface-tension forces that adhere the droplet to the substrate. Finally, these models cannot predict the critical flow strength required for droplet depinning without knowledge of the maximum droplet height and the values of the advancing and receding contact angles at the point of droplet depinning. The objective of the present work is to develop a mathematical model that addresses these limitations.

In some prior works, boundary integral methods have been applied to describe droplet behavior on a solid surface in the presence of a surrounding fluid flow.^{20–23} In some of these calculations,^{20–22} the contact-line position is fixed and a steady-state droplet shape is obtained for a given flow rate of the surrounding fluid. The flow rate beyond which a steady-state solution cannot be obtained is taken to be the critical flow rate required for droplet depinning. Transient droplet motion has been accounted for in other calculations by imposing a Navier slip condition at the contact line, although contact angle hysteresis (the difference between advancing and receding contact angles) was not included, meaning that the droplet moves for any non-zero

flow rate of the surrounding fluid.²³ Contact angle hysteresis has been accounted for in diffuse-interface/finite-volume^{24,25} and lattice-Boltzmann/finite-difference²⁶ calculations, where a point on the contact line remains stationary if the apparent contact angle θ lies within a specified range ($\theta_{rcl} < \theta < \theta_{acl}$), and moves if θ lies outside this range. As with the force-balance models, values of the advancing and receding contact angles must be specified in advance. Notably, none of the studies mentioned above explicitly account for surface roughness. Although surface roughness can be accounted for implicitly via the use of advancing and receding contact angles, accounting for it explicitly is valuable for designing surfaces and for gaining insight into the mechanics of contact-line pinning/depinning, as noted earlier.

As a first step toward addressing the limitations mentioned above, here we focus on the case of thin droplets and develop a lubrication-theory-based model for droplet depinning on a substrate with topographical defects by flow of a surrounding immiscible fluid. The droplet and surrounding fluid are in a rectangular channel, a pressure gradient is imposed to drive flow, and the defects are modeled as Gaussian-shaped bumps. Using a precursor-film/disjoining-pressure approach to capture contact-line motion, a nonlinear evolution equation is derived describing the droplet thickness as a function of distance along the channel and time. Numerical solutions of the evolution equation are used to investigate how the critical pressure gradient for droplet depinning depends on the viscosity ratio, surface wettability, droplet volume, and defect height. Simple analytical models are able to account for many of the features observed in the numerical simulations.

The paper is structured as follows. The model formulation is presented in §2, droplet dynamics on smooth substrates are explored in §3, and droplet dynamics on rough substrates and the pinning-depinning transition are investigated in §4. The influence of droplet and surrounding fluid properties on droplet depinning is discussed in §5 and the influence of substrate properties on droplet depinning is discussed in §6. Finally, residual droplet formation is studied in §7, and conclusions are presented in §8.

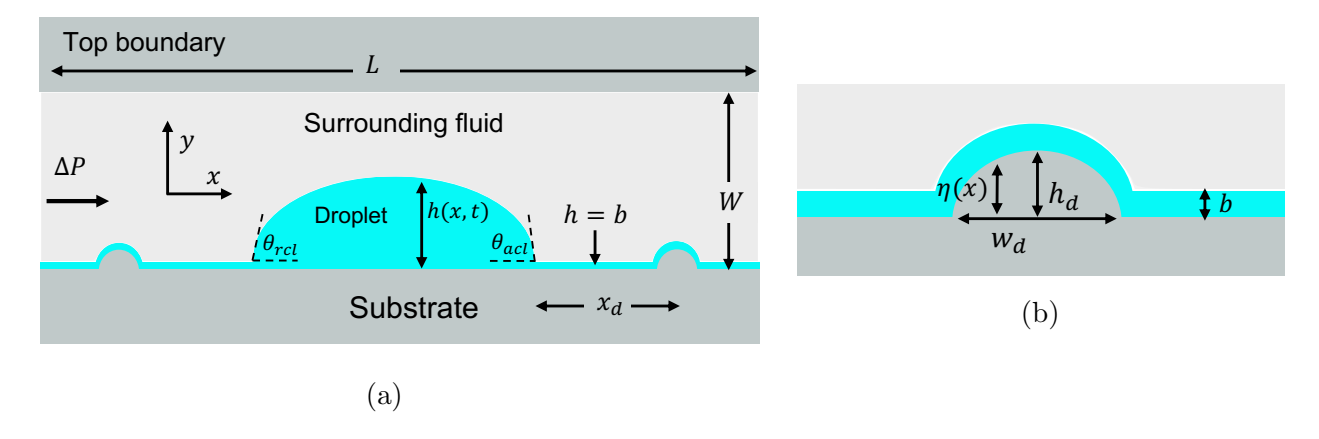


Figure 1: (a) Schematic of model geometry. (b) Enlarged view of a substrate defect.

2 Model formulation

Figure 1a shows the model geometry, where we consider a rectangular channel containing a two-dimensional Newtonian droplet surrounded by another immiscible Newtonian fluid. Here, W is the channel width, L is the channel length, h(x,t) is the droplet height, θ_{acl} is the apparent advancing contact angle, and θ_{rcl} is the apparent receding contact angle. The horizontal direction is denoted by x, the vertical direction by y, and time by t. We consider a thin droplet such that its height is much smaller than its diameter (maximum width), and we assume it is confined in a long narrow channel such that $W \ll L$. This allows us to invoke the lubrication approximation to simplify the governing equations. A negative horizontal pressure gradient of magnitude ΔP is imposed in the channel to drive flow. Although a two-dimensional droplet is actually a ridge, we refer to it as a droplet in the remainder of this paper for simplicity.

Surface roughness is incorporated by adding bump-type defects on the substrate. Figure 1b shows an enlarged view of a defect, where h_d is the maximum defect height and w_d is the maximum defect width. In practical applications, substrates can have defects of different sizes and shapes present at random locations. Here, we focus on the limiting case where a Gaussian bump-type defect is present at a distance x_d from each contact line. This reduces the complexity of the problem while allowing us to obtain physical insight into the influence of substrate topography on droplet dynamics. The substrate topography is described by the function $\eta(x) = h_d \{ \exp(-(x - x_{c1})^2/(2w_d^2)) + \exp(-(x - x_{c2})^2/(2w_d^2)) \}$, where x_{c1} is the center of the defect on the left and x_{c2} is the center of the defect on the right.

2.1 Governing equations

Several applications discussed in §1 such as crossflow microemulsification¹ and oil recovery⁴ involve long and narrow channels, which corresponds to $\epsilon = W/L \ll 1$ for our model. Consistent with lubrication theory, the maximum droplet height h_{max} is assumed to be much smaller than its diameter D, with $h_{max} \sim W$ and $D \sim L$ at most. In principle, lubrication theory requires the topography slope to be small, but in practice lubrication theory can yield qualitatively accurate predictions for two-phase problems even outside of this regime, as demonstrated by comparison to numerical simulations of the full governing equations.²⁷

The vertical and horizontal distances are non-dimensionalized with W and L, respectively. All stresses are scaled with a characteristic capillary pressure $W\sigma/L^2$, where σ is the interfacial tension.²⁸ The horizontal velocity is scaled with a capillary spreading speed $u^* = \epsilon^3 \sigma/3\mu^d$, where μ_d is the droplet viscosity, the vertical velocity is scaled with ϵu^* , and time is scaled with L/u^* .

At leading order, the mass and momentum conservation equations in each phase are:

$$u_x^i + v_y^i = 0, (2.1)$$

$$(\mu^i/\mu^d)u^i_{yy} = 3P^i_x, (2.2)$$

$$P_y^i + (\rho^i/\rho^d)Bo = 0, (2.3)$$

where the superscript i denotes the phase (i = d for droplet, and i = s for surrounding fluid), u is the horizontal velocity, v is the vertical velocity, μ is the viscosity, P is the pressure, and ρ is the density. Three dimensionless parameters arise here: (i) the Bond number $Bo = \rho^d g L^2/\sigma$, where g is the magnitude of the gravitational acceleration, which represents a ratio of gravitational forces to surface-tension forces, (ii) the viscosity ratio $\mu_r = \mu^s/\mu^d$, and (iii) the density ratio $\rho_r = \rho^s/\rho^d$. In this work, we assume $Bo \ll 1$ to isolate the influence of the imposed pressure gradient on droplet dynamics.

Motivated by prior work on droplet motion on a solid substrate, we use a precursor-film/disjoining-pressure approach to model contact-line motion. As opposed to approaches that impose a slip law on the substrate, here the contact-line position is extracted from the droplet height profile (see $\S 2.2$) and is not an extra variable, which makes the resulting equations less cumbersome to solve. This approach assumes the presence of a precursor film of thickness b along the entire substrate (Figure 1). The total pressure within

the droplet is $P = P' + \Pi$, where P' is the hydrodynamic pressure and Π is the disjoining pressure. A two-term disjoining pressure is used:

$$\Pi = A \left[\left(\frac{b}{h} \right)^n - \left(\frac{b}{h} \right)^m \right], \tag{2.4}$$

where A is the dimensionless Hamaker constant and h is the droplet thickness. The term with exponent n represents contributions from repulsive intermolecular forces, and the term with exponent m represents contributions from attractive intermolecular forces. We choose n=3 and m=2, as prior studies show that these values provide qualitatively accurate predictions of contact-line motion at a reasonable computational cost. $^{30-32}$ It should be noted that our model can be extended to incorporate chemical heterogeneity on the substrate by spatially varying $A.^{28,29,34}$

The two-term disjoining pressure determines an equilibrium contact angle of magnitude θ_{eq} , which the droplet attains in the absence of an imposed pressure gradient:²⁸

$$\theta_{eq} = \sqrt{\frac{2(n-m)Ab}{(n-1)(m-1)}}. (2.5)$$

Here, θ_{eq} is the scaled equilibrium contact angle and is related to the actual lab-frame equilibrium contact angle by $\theta_{eq,lab} = \epsilon \theta_{eq}$. All the angles discussed in the remainder of this paper are scaled angles.

The interface between the droplet and the surrounding fluid is described as $H(x,t) = h(x,t) + \eta(x)$, and we impose the following conditions:

$$u^d = u^s, (2.6)$$

$$v^d = v^s, (2.7)$$

$$P^d - P^s = -H_{xx}, (2.8)$$

$$u_y^d = \mu_r u_y^s, \tag{2.9}$$

$$h_t + \left(\int_{\eta}^H u^d \, dy\,\right)_x = 0,\tag{2.10}$$

where (2.6) and (2.7) are continuity of velocity, (2.8) is the normal stress balance, (2.9) is the tangential stress balance, and (2.10) is the kinematic condition. No-slip and no-penetration conditions are imposed at the substrate $(y = \eta(x))$ and the top boundary (y = 1):

$$u^{d}(y = \eta, t) = 0, \quad u^{s}(y = 1, t) = 0,$$
 (2.11)

$$v^{d}(y = \eta, t) = 0, \quad v^{s}(y = 1, t) = 0.$$
 (2.12)

An imposed pressure gradient in the channel generates a mean flow rate in the x-direction, and we represent its dimensionless form by Q_p . Due to mass conservation, Q_p does not vary along the x-direction, and we calculate it by considering a portion of the channel that only contains the precursor film, as it is a steady two-layer flow with a flat interface of height b,

$$Q_p = \frac{1}{4}\Delta P\left(-b^3 + \frac{3b(b-1)}{1 + (\mu_r - 1)b} + \frac{(b-1)^3}{\mu_r}\right). \tag{2.13}$$

Since the precursor-film thickness is much smaller than the channel width $(b \ll 1)$, the flow rate simplifies to $Q_p = \Delta P/4\mu_r$, which is used in the flow-rate condition:

$$\int_{\eta}^{H} u^{d} \, dy + \int_{H}^{1} u^{s} \, dy = Q_{p}. \tag{2.14}$$

We find that the qualitative nature of our results does not change if we use (2.13) in the flow-rate condition, and the quantitative difference is about 5-10%. We use the simplified flow rate here to eliminate the dependence on b.

Integrating (2.2) and (2.3) with respect to y and using conditions (2.6) - (2.14) gives the droplet height evolution equation:

$$\frac{\partial h}{\partial t} = \frac{\partial}{\partial x} \left[\frac{(H-1)^3 h^3 f(H, \mu_r, \eta)}{g(H, \mu_r, \eta)} \left(\frac{\partial H^3}{\partial x^3} + \frac{\partial \Pi_1}{\partial x} \right) + \Delta P \frac{h^3 (3 + H^2(\mu_r - 1) - 2H(1 + (\mu_r - 2)\eta + \eta(\mu_r \eta - 4)))}{4f(H, \mu_r, \eta)} \right], (2.15)$$

where

$$f(H, \mu_r, \eta) = 1 + H(\mu_r - 1) - \mu_r \eta, \tag{2.16}$$

$$g(H, \mu_r, \eta) = (H - \eta)^4 \mu_r^2 - 2\mu_r (H - 1)(H^3 - H^2(1 + 2\eta)$$

$$+ \eta(-2 + 3\eta - 2\eta^2) + H(2 - 2\eta + 3\eta^2)) + (H - 1)^4. \quad (2.17)$$

We set the length of the computational domain to L, and require the interface between the precursor film and the surrounding fluid to be flat at the left and right ends,

$$h(x = 0, t) = b, h_x(x = 0, t) = 0,$$
 (2.18)

$$h(x = L, t) = b, h_x(x = L, t) = 0.$$
 (2.19)

We use a fourth-order polynomial which satisfies (2.18) and (2.19), and specify a dimensionless droplet volume v_0 , to define the initial droplet shape. Evolution equation (2.15) is discretized using a fully implicit centered fourth-order finite-difference scheme with 6000 - 8000 spatial nodes, and the MATLAB built-in solver ode15s is used for time integration. All results were checked to ensure that they are converged with respect to spatial and temporal discretization.

In the simulations presented here, we set L=6 or L=9 to obtain results that are independent of the length of the computational domain. A value of b=0.001 is used as it allows us to recover Tanner's spreading law for a two-dimensional droplet (§3) while allowing for reasonable computation times. For all calculations with rough surfaces, the precursor film thickness is much smaller than the defect amplitude $(b/h_d \sim 10^{-2} - 10^{-1})$, indicating that the bump accounts for surface roughness in a physically realistic manner. Smaller values of b lead to slower droplet spreading and a more computationally stiff problem, but do not change the qualitative behavior of the results presented here. For many of our results, we use representative values of $v_0 = 0.2$ and $\theta_{eq} = 10^{\circ}$ (which corresponds to $A = 10^5$ using (2.5)), although we also study the effect of changing these parameters. In this paper, the largest value of θ_{eq} is 16°, which corresponds to $\tan \theta_{eq} \sim 10^{-1}$ and small interfacial slopes, consistent with the lubrication approximation.

2.2 Contact angles and contact lines

For a smooth substrate, we define apparent advancing (θ_{acl}) and receding (θ_{rcl}) contact angles (Figure 1a) as the largest angles between the substrate and the tangents to the interface between the droplet and the surrounding fluid, on the advancing and receding sides of the droplet. Advancing and receding contact-line locations, x_{acl} and x_{rcl} , are defined as the points where the tangents corresponding to the apparent contact angles and the substrate intersect. In the absence of an external pressure gradient $\theta_{acl} = \theta_{rcl}$. If $\theta_{acl} > \theta_{eq}$, the droplet spreads until $\theta_{acl} = \theta_{eq}$, and if $\theta_{acl} < \theta_{eq}$ the droplet retracts until $\theta_{acl} = \theta_{eq}$.

For substrates with topographical defects, a mesoscopic contact angle θ_m is defined, θ_m

$$\tan(\theta_m) = \frac{h_x}{1 + (h_x + \eta_x)h_x}. (2.20)$$

The apparent contact angles θ_{acl} and θ_{rcl} are obtained by finding the points on the interface between the droplet and the surrounding fluid where θ_m is the largest, on the advancing (θ_{ma} in figure 2a) and receding (θ_{mr} in figure 2b) sides of the droplet respectively, and then extrapolating the tangents at these points to the substrate. The contact-line positions x_{acl} and x_{rcl} are defined as the points where the tangents corresponding to the apparent contact angles and the substrate intersect.

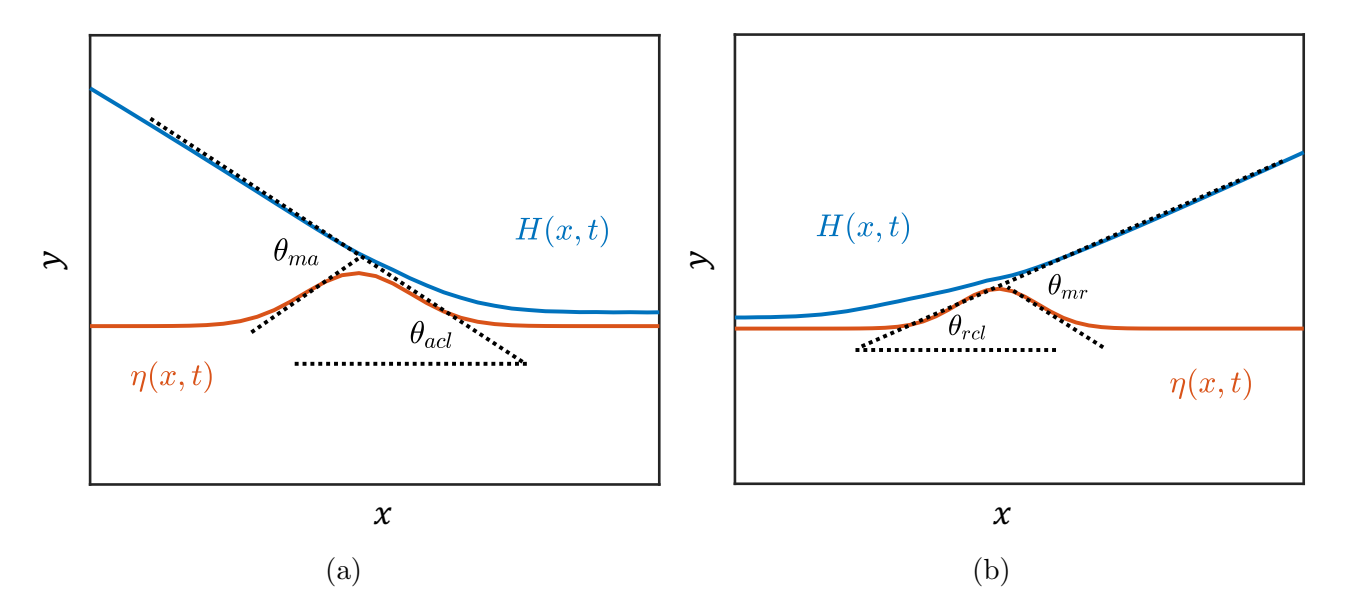


Figure 2: (a) Contact-line region when the advancing contact line moves over a defect, where η represents the substrate shape, H represents the interface shape, θ_{acl} is the apparent advancing contact angle, and θ_{ma} is the largest mesoscopic angle on the advancing half of the droplet interface. (b) Contact-line region when the receding contact line moves over a defect, where θ_{rcl} is the apparent receding contact angle, and θ_{mr} is the largest mesoscopic angle on the receding half of the droplet interface.

3 Droplet dynamics on a smooth substrate

Before considering the influence of substrate topography on droplet dynamics, we discuss the case of a smooth substrate, which corresponds to $\eta(x)=0$. We first consider the case of a droplet spreading on a substrate while surrounded by a stationary fluid ($\Delta P=0$). For perfectly wetting droplets ($\theta_{eq}=0^{o}$), our results (figure 1 of supplementary material) are consistent with Tanner's spreading law for a two-dimensional droplet ($x_{acl}-x_{c}\sim t^{1/7}$, where x_{c} is the droplet center).³⁶ This holds for all viscosity ratios we have investigated, with an increase in the surrounding-fluid viscosity simply slowing the spreading. For partially wetting droplets, viscosity has a similar effect, as seen in figure 3. The droplet spreads (x_{acl} increases and θ_{rcl} decreases) at earlier times, and eventually reaches the same steady shape for all μ_{r} since the steady droplet shape is governed by θ_{eq} .²⁸ The steady θ_{acl} ($\approx 11^{o}$) found from numerical simulations is within about 1° of the specified $\theta_{eq}=10^{o}$ from (2.5).

To study the influence of a surrounding fluid flow, we first perform a simulation such that the droplet reaches a steady shape in a stationary surrounding fluid to obtain an initial condition.

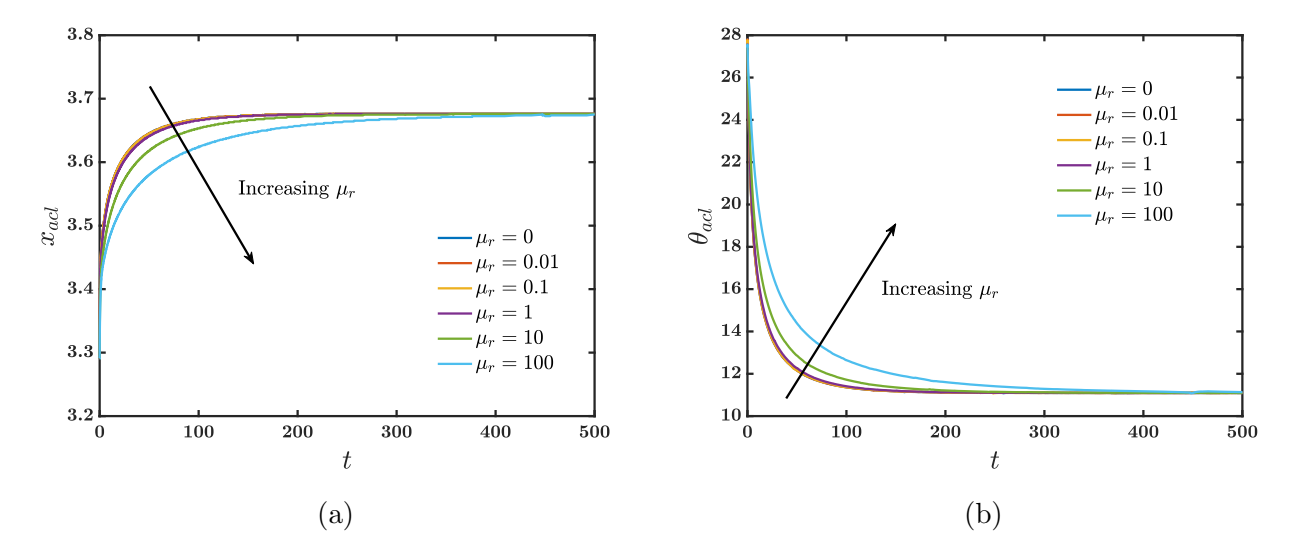


Figure 3: Droplet dynamics on a smooth substrate in a stationary surrounding fluid. (a) x_{acl} vs. t for different μ_r . (b) θ_{acl} vs. t for different μ_r . The other parameters are L = 6, $A = 10^5$ ($\theta_{eq} = 10^o$), b = 0.001, and $v_0 = 0.2$.

We then introduce a negative horizontal pressure gradient of magnitude ΔP within the channel. Figure 4a shows the variation of x_{acl} with t for different ΔP . The slope of x_{acl} vs. t at any point represents the horizontal velocity of the advancing contact line, and it is seen that this velocity reaches a steady value, which we denote as the terminal sliding velocity, v_t . Figure 4b shows the steady droplet shapes for different ΔP values. The droplet is shorter and wider for $\Delta P > 0$ compared to $\Delta P = 0$, and the deformation increases with ΔP . For a constant ΔP , additional calculations we have performed indicate that the droplet takes longer to attain a steady shape as μ_r increases. The steady shape is relatively independent of μ_r for $\mu_r \lesssim 1$, but the amount of deformation noticeably increases for sufficiently large μ_r values.

The results from the numerical simulations can be rationalized by using a flat-interface approximation, where we assume a steady pressure-driven two-layer flow with a flat interface such that the bottom layer consists of the droplet liquid and the top layer consists of the surrounding fluid. The physical variables are non-dimensionalized using the characteristic scales discussed in §2.1, and the dimensionless horizontal liquid velocity at the interface is calculated to be:

$$v_H = \frac{3\Delta P(1-H)H}{2(1+H(\mu_r - 1))},\tag{3.1}$$

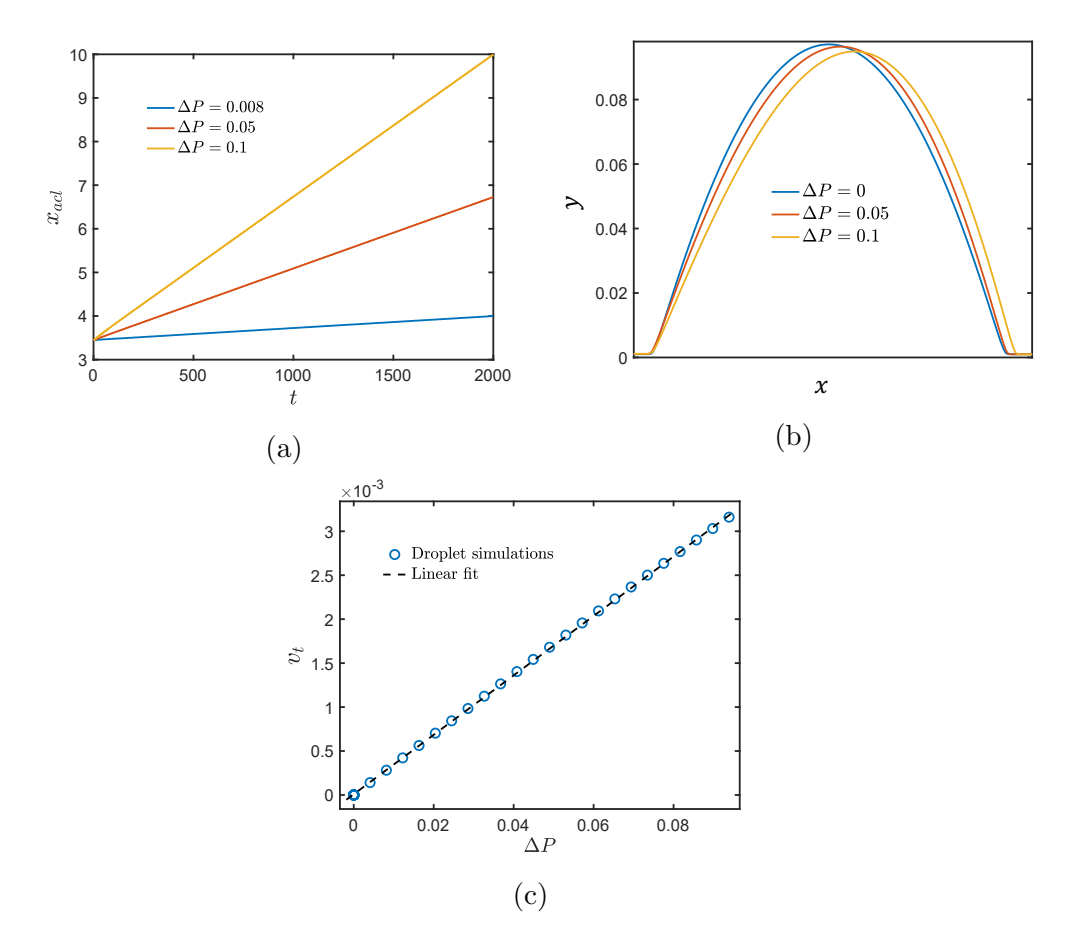


Figure 4: Droplet dynamics on smooth substrates. (a) x_{acl} vs. t for different ΔP , with $\mu_r = 0.01$ and $v_0 = 0.2$. (b) Steady droplet shapes for different ΔP on a smooth substrate. The droplet profiles have been shifted such that their receding contact lines coincide. (c) v_t vs. ΔP , with $\mu_r = 0.01$ and $v_0 = 0.2$. The other parameters are $\mu_r = 0.01$, $v_0 = 0.2$, L = 9, $A = 10^5$ ($\theta_{eq} = 10^o$), and b = 0.001.

where H is the dimensionless height of the flat interface.

For a given ΔP and μ_r , we perform a numerical simulation for a droplet to calculate v_t and the steady shape it attains, from which we extract the maximum droplet height (h_{max}) . We set $H = h_{max}$, calculate v_H using (3.1), and compare it with v_t .

Figure 4c shows that $v_t \sim \Delta P$, which is consistent with the flat-interface approximation ((3.1)). Calculating v_H from (3.1) reveals that the flat-interface approximation overpredicts v_t by a factor of about 3.6, likely because the flat-interface approximation does not account for the influence of viscous dissipation and surface-tension forces near the droplet contact line.

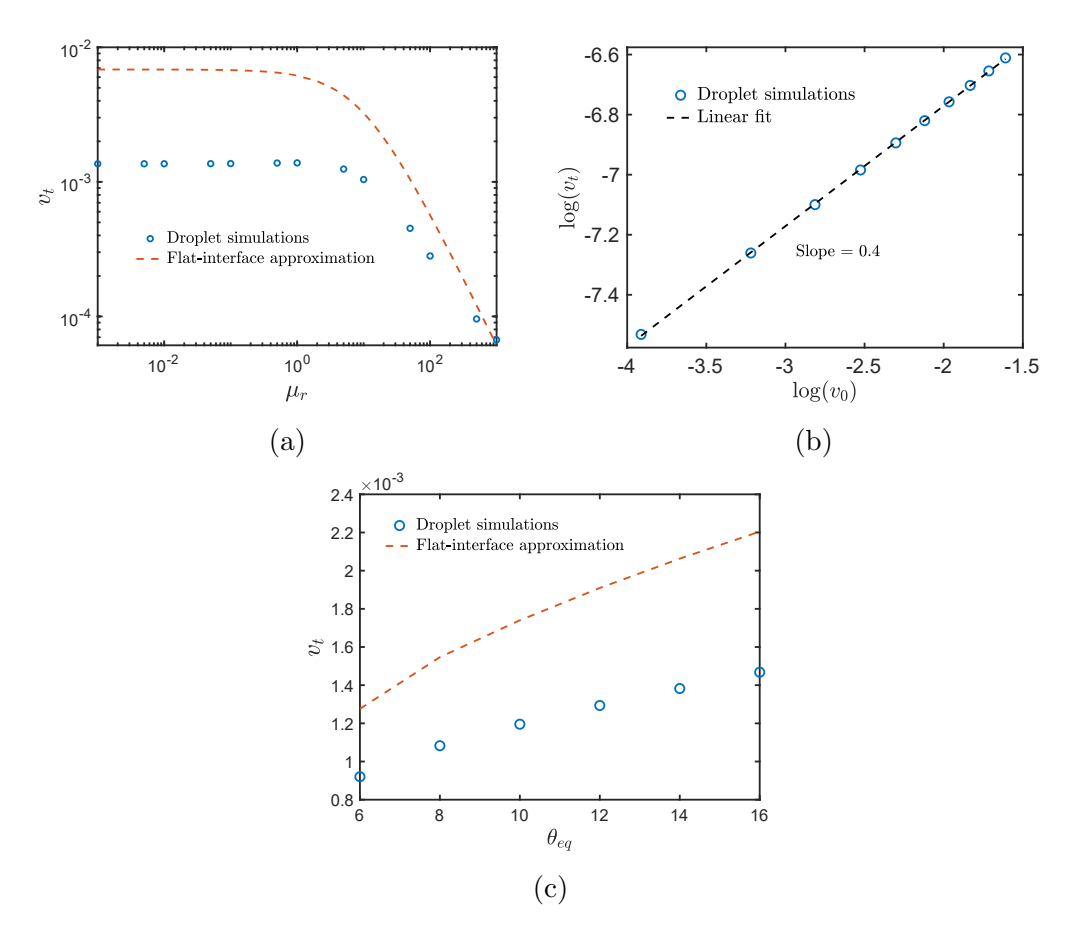


Figure 5: (a) v_t vs. μ_r , with $\Delta P = 0.04$, $A = 10^5$ ($\theta_{eq} = 10^o$), and $v_0 = 0.2$. (b) $\log(v_t)$ vs. $\log(v_0)$, with $\mu_r = 0.01$, $A = 10^5$ ($\theta_{eq} = 10^o$), and $\Delta P = 0.04$. (c) v_t vs. θ_{eq} , with $\mu_r = 0.01$, $\Delta P = 0.04$, and $v_0 = 0.2$. The other parameters are L = 9 and b = 0.001.

Figure 5a shows the variation of v_t with μ_r , where the open blue circles are results from numerical simulations for the droplet, and the dashed red line is from the flat-interface approximation (v_H) . The flat-interface approximation overpredicts v_t by nearly an order of magnitude. But it reproduces the qualitative trend observed from droplet simulations, where v_t is not strongly dependent on μ_r for $\mu_r < 1$, and decreases with μ_r for $\mu_r > 1$. This trend can be rationalized by considering (3.1). From (3.1), $v_H \approx (3H\Delta P/2)$ for $\mu_r \ll 1$, and $v_H \approx (3\Delta P(1-H)/2\mu_r)$ for $\mu_r \gg 1$. Note that for both $\mu_r \ll 1$ and $\mu_r \gg 1$, the flat-interface approximation predicts that v_H , and thus $v_t \sim \Delta P$.

To explore the effects of droplet volume, figure 5b shows $\log(v_t)$ vs. $\log(v_0)$, with v_0 being the droplet volume, for $\mu_r = 0.01$, where the open blue circles are from numerical simulations

for the droplet, and the dashed black line is a linear fit which indicates that $v_t \sim v_0^{0.4}$. Droplet simulations for $\mu_r = 100$ also yield $v_t \sim v_0^{0.4}$. Using the flat-interface approximation ((3.1)), $v_H \approx (3H\Delta P/2)$ for $\mu_r \ll 1$, and $v_H \approx (3\Delta P(1-H)/2\mu_r)$ for $\mu_r \gg 1$. This suggests that $v_t \sim h_{max}$ for the droplet, for both $\mu_r \ll 1$ and $\mu_r \gg 1$. From the simulations for both the cases, it is found that $h_{max} \sim v_0^{0.5}$ for a droplet after it attains a steady shape, and thus we obtain $v_t \sim v_0^{0.5}$, which is close to the scaling relation obtained from droplet simulations (Note that the simulations also show that the steady value of $D = x_{acl} - x_{rcl} \sim v_0^{0.5}$, consistent with mass conservation.).

Figure 5c shows v_t vs. θ_{eq} , where the open blue circles are results from numerical simulations for the droplet, and the dashed red line is from the flat-interface approximation (v_H) . The flat-interface approximation overpredicts v_t , but it reproduces the qualitative trend observed from droplet simulations. This is because h_{max} , and consequently H, increase with θ_{eq} , and v_H increases monotonically with H as can be seen by analyzing (3.1). Although it misses important details, the flat-interface approximation is also useful for understanding droplet dynamics on rough substrates, as will be shown later.

4 Droplet dynamics on a rough substrate

In this section, we study the influence of substrate topography. To obtain an initial condition for a given set of parameters, we perform a numerical simulation such that the droplet reaches a steady shape on a smooth substrate in a stationary surrounding fluid, then add a Gaussian bump-type defect (discussed in §2) at each contact line with $x_d = 0$ (Figure 1a) to pin the droplet. We then introduce a negative horizontal pressure gradient of magnitude ΔP in the channel. For the calculations presented in this section we fix $h_d = 0.02h_{max}$ and $w_d = 2h_d$ to isolate the effects of ΔP . The influence of defect geometry on droplet dynamics is discussed in §6.2.

4.1 Pinning-depinning transition

Figures 6a and 6b show the variation of θ_{acl} and x_{acl} with t for $\Delta P = 0.05$ and $\Delta P = 0.07$. For $\Delta P = 0.05$, x_{acl} does not vary with t, and θ_{acl} increases with t to eventually reach a steady value. This behavior is indicative of droplet pinning. For $\Delta P = 0.07$, θ_{acl} increases with t and x_{acl} remains constant until t = 266. Then, for t > 266, θ_{acl} decreases with t and eventually

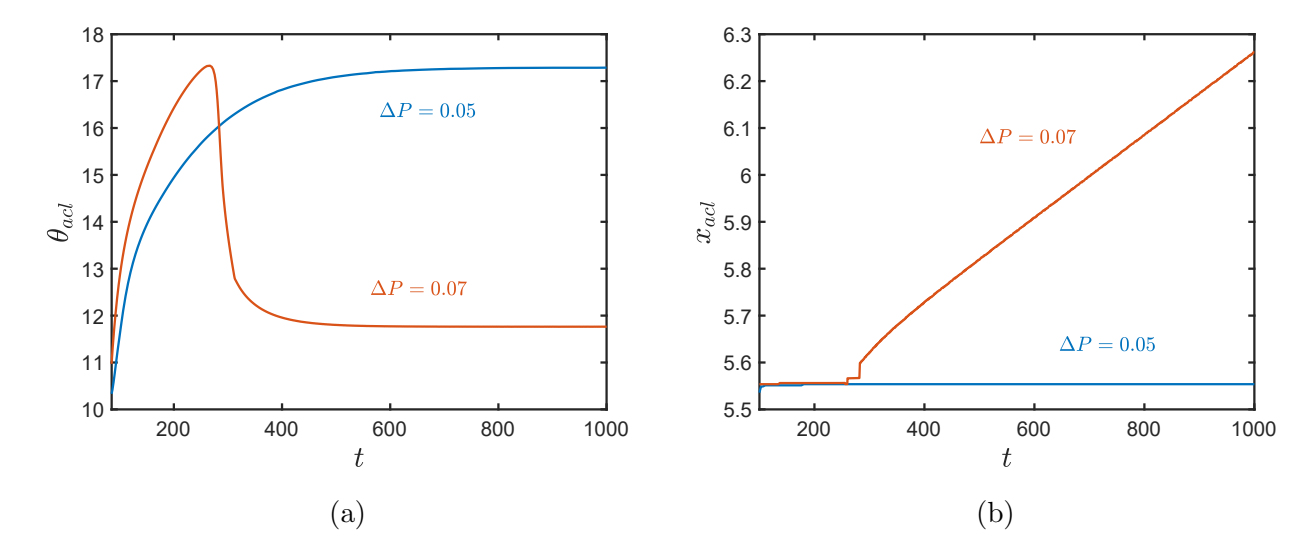


Figure 6: Droplet dynamics on a rough substrate. (a) θ_{acl} vs. t. (b) x_{acl} vs. t. The kinks in x_{acl} at t = 266 indicate that the contact line rapidly depins from the defect at that time and shifts to the right. The smaller kink to the left of the larger kink arises while numerically resolving x_{acl} from droplet profiles. The other parameters are L = 9, $\mu_r = 0.01$, $A = 10^5$ ($\theta_{eq} = 10^o$), b = 0.001, $v_0 = 0.2$, $h_d = 0.02h_{max}$, and $w_d = 2h_d$.

reaches a steady value, and x_{acl} increases with t. This behavior is indicative of droplet depinning. Overall, these results suggest that there is a critical ΔP above which droplet depinning occurs.

Figure 7a shows the variation of the steady θ_{acl} value with ΔP , and it is seen that θ_{acl} increases with ΔP for $\Delta P < 0.063$. For $\Delta P < 0.063$, it is found that x_{acl} remains equal to its initial value, similar to what is seen for $\Delta P = 0.05$ (blue line in figure 6b). As ΔP increases from zero, the droplet remains pinned but becomes increasingly deformed, as shown in figure 7b.

At $\Delta P = 0.063$, a significant decrease in θ_{acl} is observed, indicating droplet depinning, and for $\Delta P > 0.063$, there is a slight increase in θ_{acl} with ΔP . Furthermore, for $\Delta P > 0.063$, the behavior of x_{acl} as a function of t is qualitatively similar to that for $\Delta P = 0.07$ (red line in figure 6b), where x_{acl} remains equal to the initial value for a period of time and then gradually increases with t. Thus, after the droplet depins it slides on the substrate with a steady shape, as shown in figure 7c (see supplementary material for videos of droplet pinning and depinning).

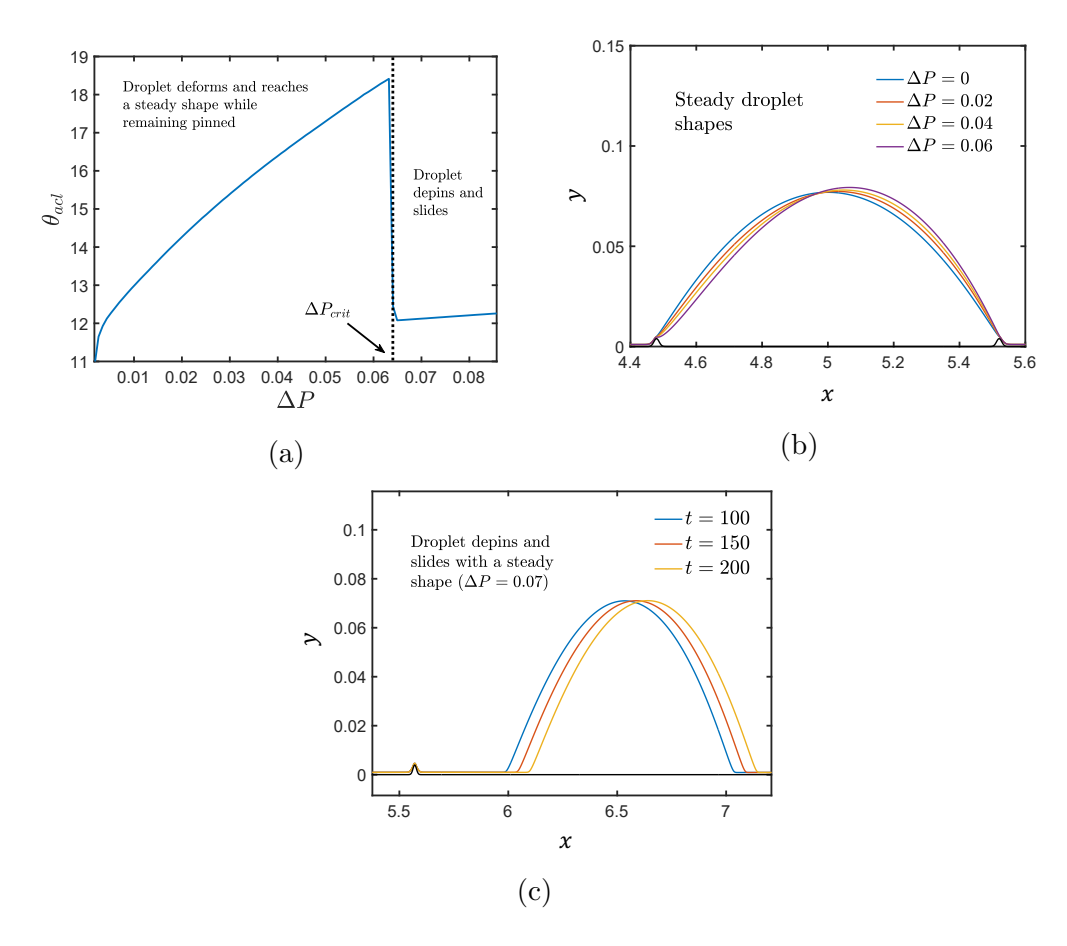


Figure 7: (a) Steady value of θ_{acl} vs. ΔP . (b) Steady droplet profiles for different ΔP . (c) Droplet profiles at different t for $\Delta P = 0.07$. The solid black lines show substrate topography and the other lines show droplet profiles. All other parameters are the same as in figure 6.

4.2 Droplet pinning mechanism

As discussed in §1, the pinning-depinning transition has been rationalized in prior work using simple force-balance models. ^{10,12} We apply those ideas here to see how well they describe our results. In those models, the drag force acting on the droplet due to the surrounding fluid flow drives depinning, and the surface-tension force acting along the droplet contact line resists depinning. The total drag force acting on the droplet is predominantly composed of skin drag and the pressure drag is negligible. Also, the total drag force is nearly equal to the shear force due to the droplet being thin (figure 2 of supplementary material). We note that pressure drag is expected to become significant for droplets not well described by the lubrication approximation. The balance between the shear force and the surface-tension force

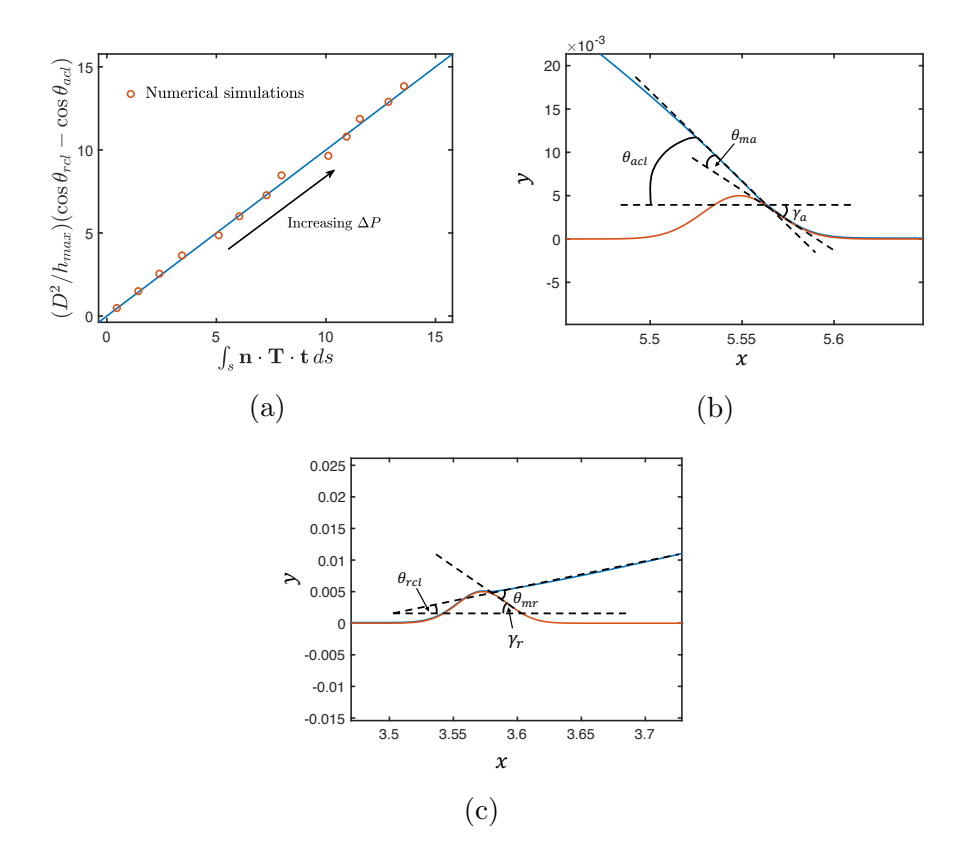


Figure 8: (a) Terms in the force-balance model for pinned droplets at different ΔP values. The open red circles are results from numerical simulations and the straight blue line has a slope of unity. (b) Enlarged view of the pinned advancing contact line for $\Delta P = 0.03$, where the blue line shows the droplet and the red line shows the defect. (c) Enlarged view of the pinned receding contact line for $\Delta P = 0.03$, where the blue line shows the droplet and the red line shows the defect. The other parameters are L = 9, $\mu_r = 0.01$, $A = 10^5$ ($\theta_{eq} = 10^o$), b = 0.001, $v_0 = 0.2$, $h_d = 0.02h_{max}$, and $w_d = 2h_d$.

can be represented in a dimensionless form as $(D^2/h_{max})(\cos\theta_{rcl} - \cos\theta_{acl}) \sim \int_s \mathbf{n} \cdot \mathbf{T} \cdot \mathbf{t} \, ds$ (see appendix). Here, $D = x_{acl} - x_{rcl}$ is the droplet width, h_{max} is the maximum droplet height, \mathbf{n} is the unit normal vector at the interface between the droplet and the surrounding fluid that points into the surrounding fluid, \mathbf{T} is the droplet stress tensor, \mathbf{t} is the unit tangent vector at the interface, and s is the interface arclength coordinate such that s = 0 at the receding contact line and s = 1 at the advancing contact line.

We extract the values of D, h_{max} , θ_{acl} , θ_{rcl} , \mathbf{n} , \mathbf{T} , and \mathbf{t} from the steady droplet shapes in numerical simulations to calculate the terms in the force balance. Figure 8a shows these terms for different $\Delta P < \Delta P_{crit}$, with the open red circles presenting the simulation results. As can

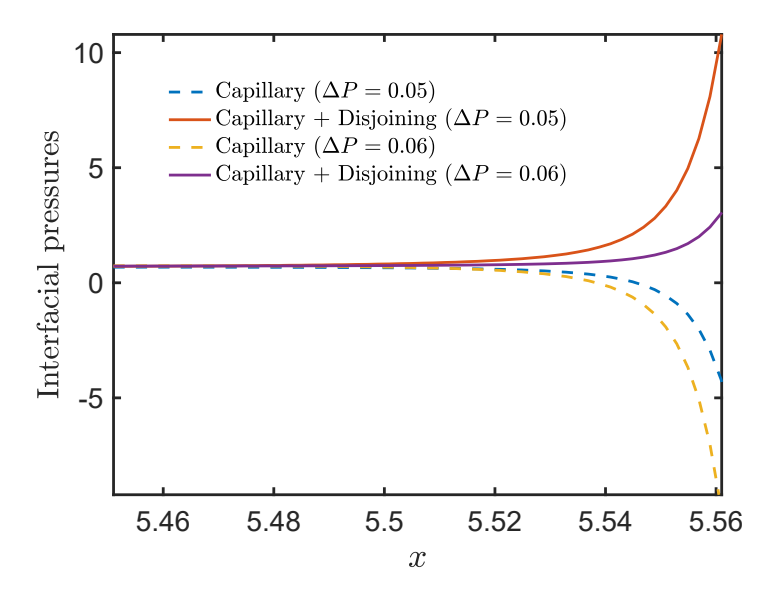


Figure 9: Droplet pressure vs. x for a pinned droplet ($\Delta P = 0.05$). The dashed blue line shows the contribution from the capillary pressure and the solid red line shows the total pressure (capillary and disjoining). All the other parameters are the same as in figure 8.

be seen, there is indeed a linear relationship, consistent with the force-balance model. It should be noted that inertial forces may become important for larger droplets or larger ΔP values,³⁷ but they are neglected in this work.

Next, we discuss the pinning locations of the two contact lines. It can be seen from figures 8b and 8c that the following geometric relations hold at the pinned advancing and receding contact lines:

$$\theta_{acl} = \theta_{ma} + \gamma_a, \tag{4.1}$$

$$\theta_{rcl} = \theta_{mr} - \gamma_r, \tag{4.2}$$

where γ_a is the magnitude of the slope at the point on the defect on the right that coincides with x_{acl} , and γ_r is the magnitude of the slope at the point on the defect on the left that coincides with x_{rcl} . Our calculations show that for all the cases of a pinned droplet, $\theta_{ma} \approx \theta_{mr} \approx \theta_{eq}$, so the values of θ_{rcl} and θ_{acl} depend primarily on γ_r and γ_a , respectively.

For all the cases where the droplet is pinned, it is found that x_{rcl} and x_{acl} coincide with the points on the defects where there is a maximum negative slope, whose magnitude we denote as γ_{max} . Using (4.1) and (4.2), it can be seen that as a consequence of these pinning locations,

 $\theta_{rcl} \approx \theta_{eq} - \gamma_{max}$ is minimized, and $\theta_{acl} \approx \theta_{eq} + \gamma_{max}$ is maximized, which maximizes the surface-tension term in the force-balance model $(D^2/h_{max})(\cos\theta_{rcl} - \cos\theta_{acl})$. These findings are consistent with predictions from a lubrication-theory-based model for a droplet sliding down an inclined substrate with a single Gaussian-shaped bump, where the advancing contact line pins at the point on the bump that has the maximum negative slope, as it maximizes the surface-tension force.³⁵ The present work shows that similar behavior occurs even in more complicated situations, where the geometry and driving force for flow are different, and the dynamics of both phases are accounted for.

The pinning-depinning transition can also be understood through an analysis of the pressure gradients in the droplet. 30,32 Figure 9 shows the variation of the pressure in a pinned droplet with x for two ΔP values. The total pressure includes contributions from the capillary pressure and the disjoining pressure, and figure 9 shows the former quantity as well. For each case, the capillary pressure has a negative gradient and drives flow from the droplet interior toward the advancing contact line (located at x = 5.56), which promotes depinning. But the disjoining pressure increases closer to the contact line, and causes the total pressure gradient within the droplet to become positive, which drives flow from the advancing contact line toward the droplet interior. Near the receding contact line, the total pressure gradient within the droplet is negative (figure 3 of supplementary material), which drives flow from the receding contact line toward the droplet interior. The flows near the two contact lines oppose each other and result in a pinned droplet.

As ΔP increases, the pinned droplet becomes increasingly deformed (see figure 7b), which increases the droplet thickness near the advancing contact line and decreases the disjoining pressure there. As a result, the total pressure gradient near the advancing contact line decreases as shown in figure 9. At ΔP_{crit} , the total pressure gradient near the advancing contact line becomes negative, and the total pressure gradient near the receding contact line remains negative. This results in a net negative pressure gradient within the droplet, which causes the two contact lines to depin simultaneously, and the droplet slides to the right.

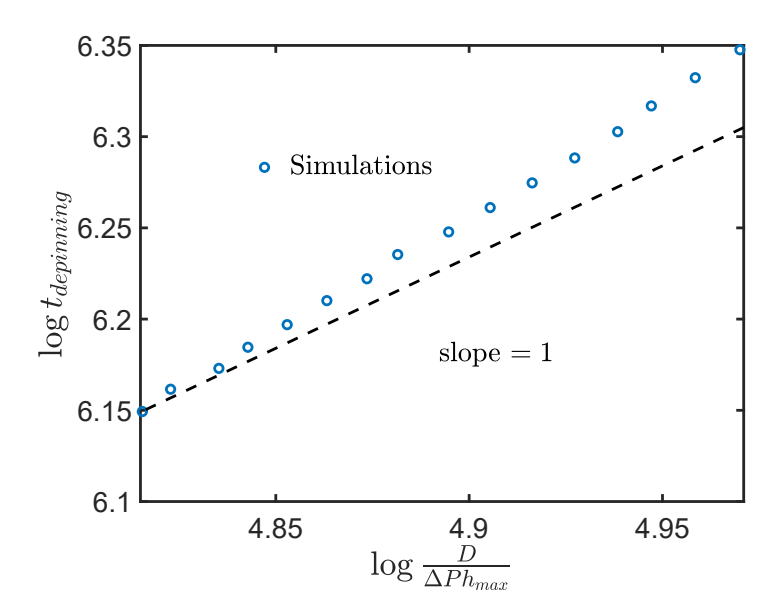


Figure 10: $\log t_{depinning}$ vs. $\log D/(\Delta P h_{max})$, where the open blue circles show calculations from numerical simulations, and the dashed black line shows a slope of 1. The other parameters are L=9, $\mu_r=0.01$, $A=10^5$ ($\theta_{eq}=10^o$), b=0.001, $v_0=0.2$, $h_d=0.02h_{max}$, and $w_d=2h_d$.

4.3 Droplet depinning time

The time it takes the droplet to depin when $\Delta P > \Delta P_{crit}$ is of both fundamental and practical interest. The droplet depinning time, $t_{depinning}$, is calculated as the time at which the receding contact line position, x_{rcl} , crosses the defect on the right. A scaling relation can be obtained for $t_{depinning}$ by dividing the droplet width, D, with the droplet velocity (3.1) obtained from the flat-interface approximation (§3). For $\mu_r \ll 1$, this yields $t_{depinning} \sim D/\Delta P h_{max}$.

Figure 10 shows $\log t_{depinning}$ vs. $\log D/(\Delta P h_{max})$, where the open blue circles are calculations from numerical simulations and the dashed black line has a slope of 1. The intercept for the dashed black line is chosen such that it overlaps with the simulation result at $\log D/(\Delta P h_{max}) = 4.1814$. Fitting a straight line to the numerical calculations yields a slope of 1.423. Thus, the scaling law derived above predicts a faster depinning time $(\sim D/(\Delta P h_{max}))$ than what is observed from numerical simulations $(\sim (D/(\Delta P h_{max}))^{1.423})$. This is expected based on the results in §3, as the flat-interface approximation does not account for viscous dissipation and surface-tension forces near the contact lines, which slow down droplet motion.

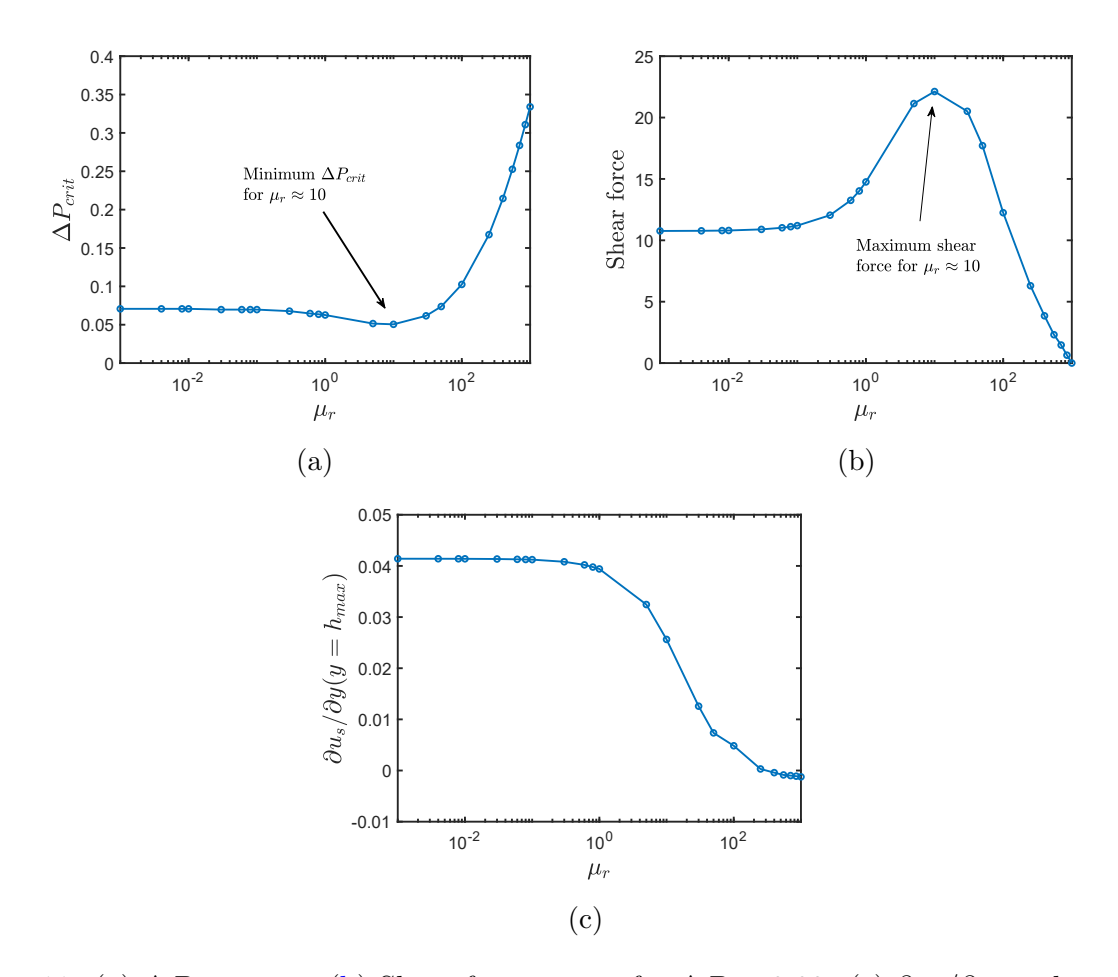


Figure 11: (a) ΔP_{crit} vs. μ_r (b) Shear force vs. μ_r for $\Delta P = 0.03$. (c) $\partial u_s/\partial y$ at the maximum height of pinned droplet vs. μ_r for $\Delta P = 0.03$. The other parameters are L = 9, $\mu_r = 0.01$, $A = 10^5$ ($\theta_{eq} = 10^o$), b = 0.001, $v_0 = 0.2$, $h_d = 0.02h_{max}$, and $w_d = 2h_d$.

5 Influence of droplet and surrounding fluid properties on the critical pressure gradient

5.1 Influence of viscosity ratio

Figure 11a shows ΔP_{crit} vs. μ_r . For $\mu_r < 1$, ΔP_{crit} decreases slightly with μ_r , and this result is qualitatively consistent with the experimental observations of Fan et al.,¹² where as the viscosity of the glycerol-water droplet increases (by increasing the glycerol concentration), a larger critical flow rate of the surrounding air is required to depin it on a treated glass surface. For $\mu_r > 1$, ΔP_{crit} decreases with μ_r to reach a minimum value at $\mu_r \approx 10$, and then increases with μ_r . These results can be rationalized by examining the shear force acting on the droplet.

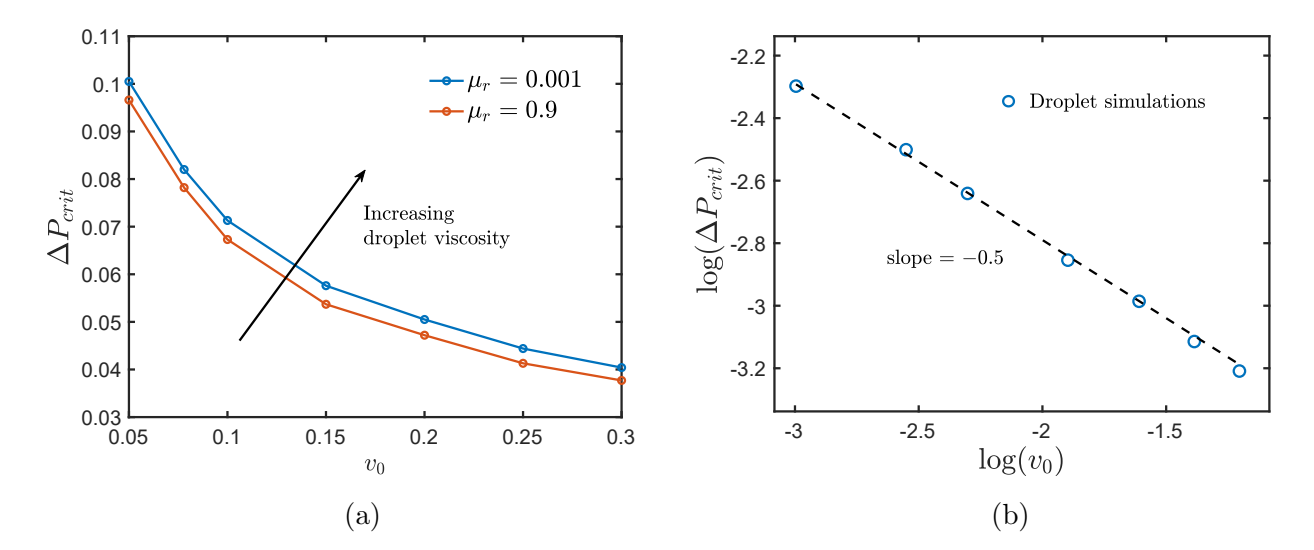


Figure 12: (a) ΔP_{crit} vs. v_0 for $\mu_r = 0.001$ and $\mu_r = 0.9$ (b) $\log \Delta P_{crit}$ vs. $\log v_0$ for $\mu_r = 0.001$, where the open blue circles show calculations from droplet simulations, and the dashed black line shows a linear fit with a slope of -0.5. The other parameters are L = 9, $A = 10^5$ ($\theta_{eq} = 10^o$), b = 0.001, $h_d = 0.02h_{max}$, and $w_d = 2h_d$.

Our calculations show that the surface-tension force does not vary significantly with μ_r ($\approx 6\%$), so we do not consider it here.

Figure 11b shows shear force vs. μ_r for a fixed $\Delta P < \Delta P_{crit}$. Using lubrication theory, the shear force $\int_s \mathbf{n} \cdot \mathbf{T} \cdot \mathbf{t} \, ds$ simplifies to $\int_s \mu_r \partial u_s / \partial y \, ds$, where $\partial u_s / \partial y$ is the horizontal velocity gradient with respect to y in the surrounding fluid at the interface. For a constant ΔP , as μ_r increases, the surrounding fluid becomes more viscous and exerts a larger shear force on the droplet. But for $\mu_r \gg 1$, the surrounding fluid becomes so viscous that the net flow rate along the x-direction decreases. Consequently, $\partial u_s / \partial y$ decreases with μ_r as exemplified in figure 11c, where $\partial u_s / \partial y$ at the maximum height of the pinned droplet is shown. As a result, the shear force decreases with μ_r for $\mu_r \gg 1$, and the droplet experiences a maximum shear force, and consequently a minimum ΔP_{crit} for $\mu_r \approx 10$. This observation is potentially important for applications such as crossflow microemulsification and oil recovery, where the viscosity of the surrounding fluid could be tuned to minimize ΔP_{crit} .

5.2 Influence of droplet volume

Figure 12a shows ΔP_{crit} vs. v_0 for two different values of $\mu_r < 1$ (droplet more viscous than the surrounding fluid). It is seen that ΔP_{crit} decreases with v_0 for each case, and a larger

 ΔP_{crit} is required for a smaller μ_r . This result is qualitatively consistent with the experimental findings of Fan et al., where a lower critical flow rate of surrounding air is required to depin a larger glycerol-water droplet on a treated glass surface, and a larger flow rate is required to depin a more viscous droplet of the same volume.¹² For $\mu_r > 1$, ΔP_{crit} decreases with v_0 as well (figure 4 of supplementary material).

These results can be understood in terms of the force-balance model discussed in §4.2. An analytical expression is obtained for the shear force acting on the droplet using the flat-interface approximation (see §3), where the shear stress acting on a flat interface of height H is multiplied by the length of the horizontal domain L:

$$F_s^{flat} = 3\Delta PL \left(H - \frac{1 + H^2(\mu_r - 1)}{2(1 + H(\mu_r - 1))} \right). \tag{5.1}$$

Using (5.1) to calculate the shear force by setting $H = h_{max}$ obtained from the steady droplet profiles, and assuming $L \sim D$, the dimensionless force balance at the point of depinning can be expressed as $3\Delta P_{crit}$ $(h_{max}-1)/2 \sim (D/h_{max}(\cos\theta_{rcl}-\cos\theta_{acl}))$ for $\mu_r \ll 1$, and $3\Delta P_{crit}h_{max}/2 \sim (D/h_{max})(\cos\theta_{rcl}-\cos\theta_{acl})$ for $\mu_r \gg 1$. As discussed in §3, both D and $h_{max} \sim v_0^{0.5}$. Thus, $\Delta P_{crit} \sim v_0^{-0.5}$ for both $\mu_r \ll 1$ and $\mu_r \gg 1$. Figure 12b shows $\log \Delta P_{crit}$ vs. $\log v_0$ for $\mu_r = 0.001$, where the open blue circles are results from numerical simulations and the dashed black line shows a slope of -0.5. The close agreement indicates that the flat-interface approximation accurately captures the influence of v_0 on ΔP_{crit} . Results from numerical simulations for $\mu_r = 100$ follow the scaling relation as well (figure 4 of supplementary material).

6 Influence of substrate properties on droplet depinning

6.1 Influence of substrate wettability

Figure 13a shows ΔP_{crit} vs. θ_{eq} for $\mu_r = 0.01$, and it is seen that ΔP_{crit} increases with θ_{eq} . This result is qualitatively consistent with the experimental findings of Madani and Amirfazli,⁹ where a lower surrounding water flow rate is required to depin an oil droplet ($\mu_r < 1$) on a more wettable substrate.

These results can be understood by examining the surface-tension term in the force-balance model, $(D^2/h_{max})(\cos\theta_{rcl}-\cos\theta_{acl})$ (see §4.2), which increases with θ_{eq} as shown in figure 13b. The shear force acting on the droplet is not considered as it does not vary significantly with

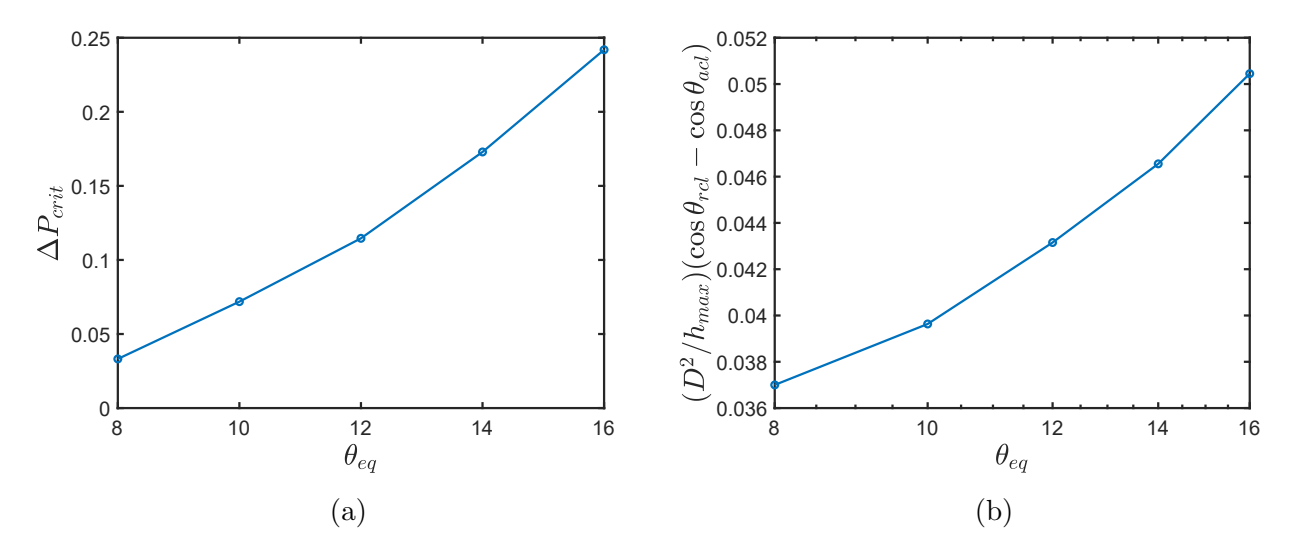


Figure 13: (a) ΔP_{crit} vs. θ_{eq} . (b) $(D^2/h_{max})(\cos\theta_{rcl} - \cos\theta_{acl})$ vs. θ_{eq} for $\Delta P = 0.03$. The other parameters are L = 9, $\mu_r = 0.01$, $v_0 = 0.2$, b = 0.001, $h_d = 0.02h_{max}$, and $w_d = 2h_d$.

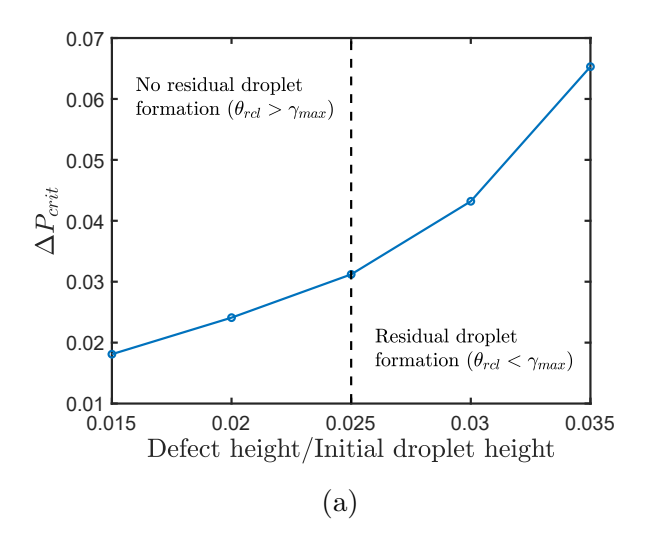
 θ_{eq} ($\approx 7\%$). This can be understood from the flat-interface approximation. According to (5.1), the shear force depends on h_{max} , which does not vary significantly with θ_{eq} ($\approx 8\%$).

As θ_{eq} increases, $\theta_{rcl} \approx \theta_{eq} - \gamma_{max}$ increases, which tends to decrease the surface-tension force. Additionally, $\theta_{acl} \approx \theta_{eq} + \gamma_{max}$ increases, which tends to increase the surface-tension force. Overall, a net increase is observed in the surface-tension force (figure 13b), and a larger ΔP_{crit} is required for droplet depinning on a less wettable substrate.

6.2 Influence of defect geometry

The defect shape is governed by its maximum height h_d and maximum width w_d (see §2). It can be seen from figure 1b that the maximum slope along the defect γ_{max} increases with h_d (constant w_d), and decreases with w_d (constant h_d). As will be discussed below, ΔP_{crit} depends only on γ_{max} , and increasing h_d has the same qualitative effect on droplet dynamics as decreasing w_d . Here, we vary h_d while keeping w_d constant.

Figure 14a shows ΔP_{crit} vs. the ratio of h_d to the initial maximum droplet height, and it is seen that ΔP_{crit} increases with h_d . This result can be understood by examining the surface-tension force acting along the contact line. As discussed in §6.1, the shear force acting on the droplet for a fixed ΔP depends on h_{max} , which does not vary significantly with h_d ($\approx 4\%$), and μ_r , which does not vary with h_d . As a consequence, the shear force does not vary significantly with h_d ($\approx 6\%$).



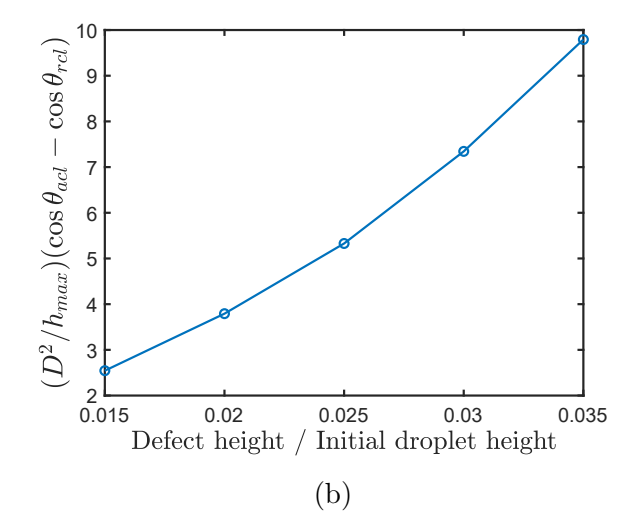


Figure 14: (a) ΔP_{crit} vs. h_d . (b) $(D^2/h_{max})(\cos\theta_{rcl} - \cos\theta_{acl})$ vs. θ_{acl} for $\Delta P = 0.015$. The other parameters are L = 9, $\mu_r = 0.01$, b = 0.001, $A = 10^5$ ($\theta_{eq} = 10^o$), $v_0 = 0.2$, and $w_d = 0.008$.

As discussed in §4.2, $\theta_{acl} \approx \theta_{eq} + \gamma_{max}$ and $\theta_{rcl} \approx \theta_{eq} - \gamma_{max}$. It can be seen that for a fixed θ_{eq} , as h_d , and consequently γ_{max} , increases, θ_{acl} increases and θ_{rcl} decreases. As a result, the surface-tension term in the force-balance model $(D^2/h_{max})(\cos\theta_{rcl} - \cos\theta_{acl})$ increases with h_d , as shown in figure 14b. Thus, a larger ΔP_{crit} is required for droplet depinning if taller defects are present on the substrate. Similarly, a larger ΔP_{crit} is required for narrower defects (figure 5 of supplementary material).

We also find that when the ratio of the defect height to the initial maximum droplet height is greater than 0.025 (see dashed line in figure 14a), smaller residual droplets are formed behind and in front of the defect on the right, after the original droplet depins. (The value of 0.025 is specific to the parameters used in the calculations.) We discuss this phenomenon in the next section.

7 Residual droplet formation

7.1 Geometric mechanism

Figure 15 shows droplet profiles as time progresses after the droplet depins, and it is seen that a residual droplet is formed behind the defect on the right as the droplet slides over it. This happens when $\theta_{rcl} < \gamma_{max}$ as the receding contact line approaches the defect. The disjoining

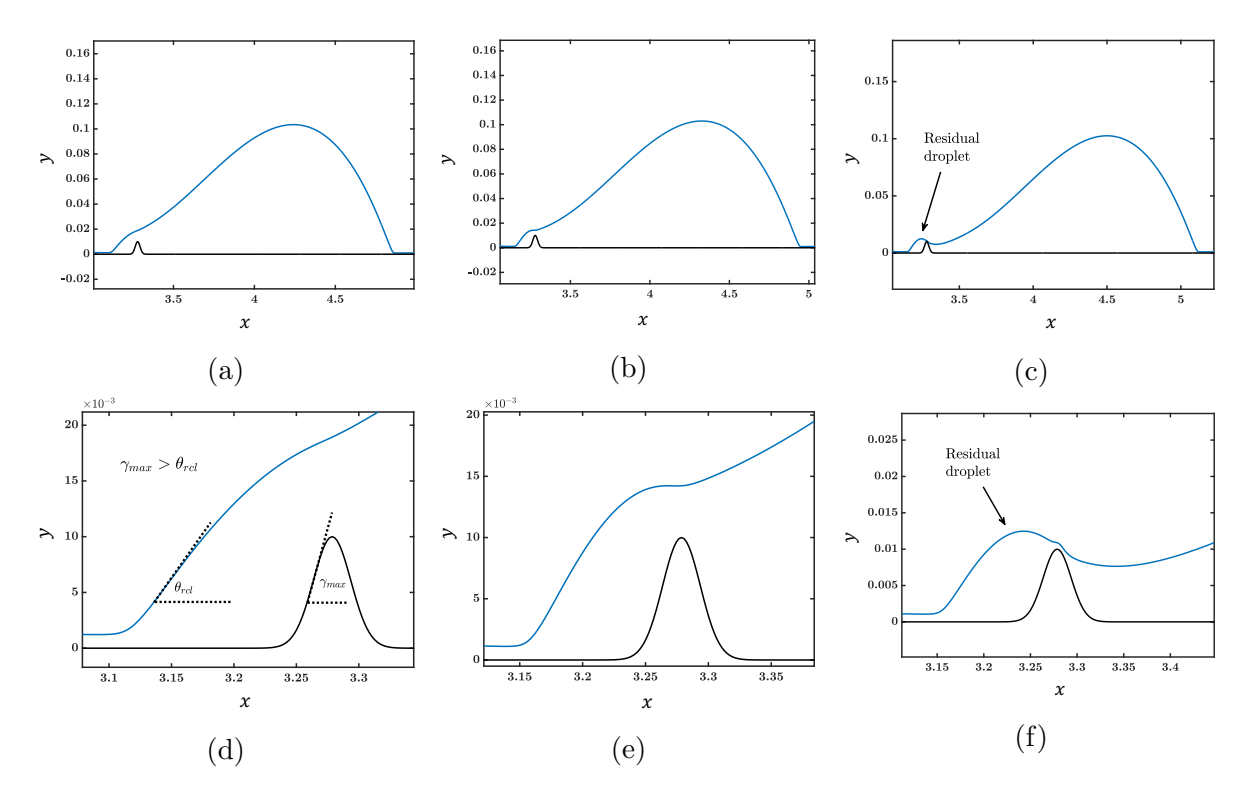


Figure 15: Droplet profiles at (a) t = 500 (b) t = 520 and (c) t = 540. Enlarged view of the contact line at (d) t = 500 (e) t = 520 and (f) t = 540. The solid black lines show substrate topography and the blue lines show droplet profiles. The parameters are L = 9, $A = 10^5$ ($\theta_{eq} = 10^o$), $v_0 = 0.2$, b = 0.001, $\Delta P = 0.1$, $h_d = 0.02h_{max}$, and $w_d = 2h_d$.

pressure above the defect increases due to droplet thinning, which drives flow away from this region and a smaller residual droplet is pinched-off behind the defect. But if $\theta_{rcl} > \gamma_{max}$, the droplet slides over the defect without leaving behind a residual droplet. It should be noted that θ_{rcl} is obtained as an output from our calculations (see §2.2) and generally depends on the viscosity ratio, droplet volume, substrate wettability, and defect geometry. These findings are consistent with a prior lubrication-theory-based model for a droplet sliding down an inclined substrate with a single Gaussian-shaped bump, where a residual droplet is formed behind the bump, if $\theta_{rcl} < \gamma_{max}$ as the receding contact line approaches the bump.³⁵

It is also found that an additional residual droplet forms in front of the defect at later times if $\theta_{rcl} < \gamma_{max}$. Figure 16 shows droplet profiles as time progresses after the formation of the residual droplet behind the defect. As seen in figure 15, the receding contact line remains in the vicinity of the defect during the pinch-off of the residual droplet behind the defect, while

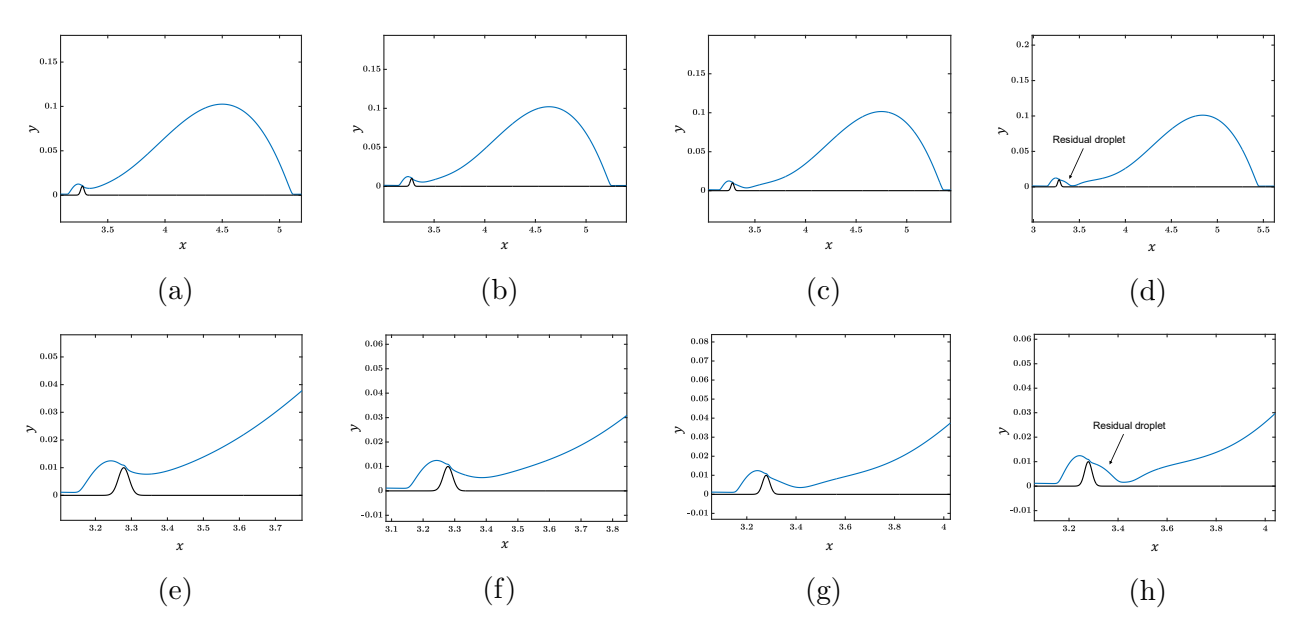


Figure 16: Droplet profiles at (a) t = 560 (b) t = 580 (c) t = 600 and (d) t = 620. Enlarged view of the contact line at (e) t = 560(f) t = 580 (g) t = 600 and (h) t = 620. The solid black lines show substrate topography and the blue lines show droplet profiles. The parameters are the same as in figure 15.

the advancing contact line slides to the right. As a result, the droplet elongates and attains a slender concave upward shape on its receding side to the right of the defect as shown in figures 16a and 16e. Consequently, the disjoining pressure in this region increases, which drives flow away from the thinnest point of the interface, and a smaller residual droplet is pinched-off in front of the defect (figures 16b-16d and 16f-16h). These findings are also consistent with the prior work discussed above on droplets sliding down an inclined substrate, indicating that the condition for residual droplet formation ($\theta_{rcl} < \gamma_{max}$) holds more generally. Indeed, one would expect this criterion to hold for a broad range of geometries and flows as long as the topography amplitude is much smaller than the length scales characterizing the overall flow. We note that increasing the droplet volume increases the value of θ_{rcl} when the receding contact line encounters the defect, eventually leading to $\theta_{rcl} > \gamma_{max}$ and suppression of residual droplet formation.

The formation of residual droplets has important implications for practical applications. Our results indicate that the presence of topographical defects on the substrate may make it difficult to recover the entire volume of the droplet in applications such as surface cleaning

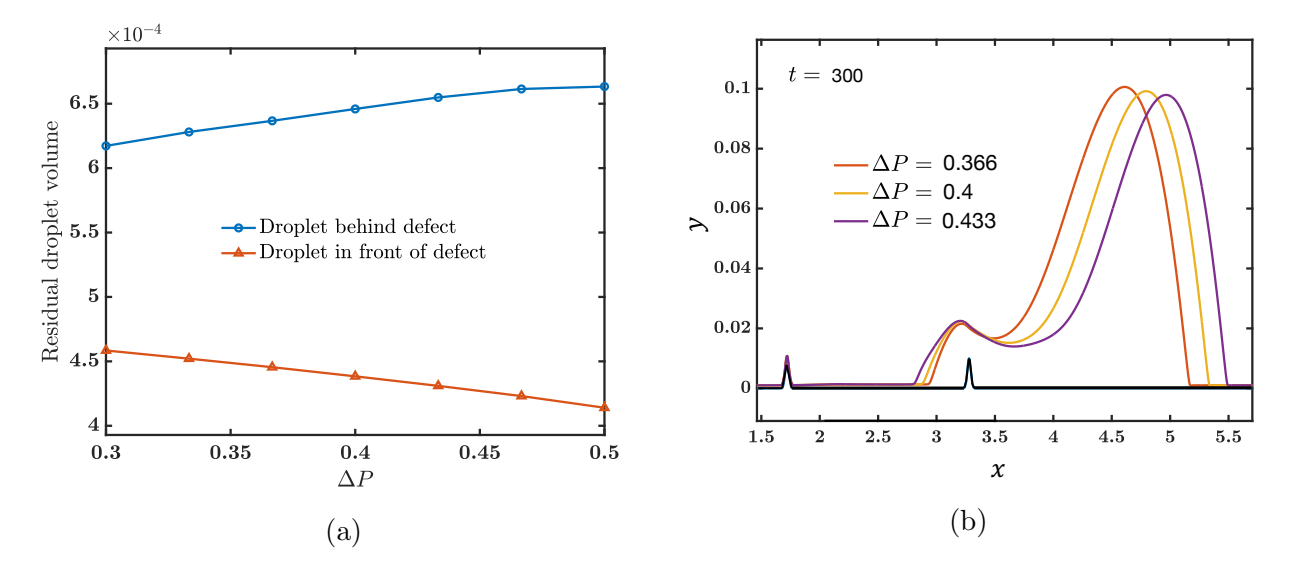


Figure 17: (a) Residual droplet volume vs. ΔP . (b) Droplet profiles at t=300 for different ΔP values. The solid black line shows substrate topography and the other lines show droplet profiles. The parameters are L=9, $A=10^5$ ($\theta_{eq}=10^o$), $v_0=0.2$, b=0.001, $\Delta P=0.1$, $h_d=0.02h_{max}$, and $w_d=2h_d$.

and oil recovery. But for applications such as microemulsification, our results suggest that the size of the dispersed phase droplets could be controlled by designing defects to break-up larger droplets into smaller ones.

7.2 Influence of pressure gradient on residual droplet volume

We now consider the influence of ΔP on the volume of the residual droplets formed at the defect. The volume of a residual droplet is calculated as $\int_{x_l}^{x_r} h \, dx$, where x_l and x_r are the left and right end points of the residual droplet. These values are calculated such that $h > b \, \forall x_l < x < x_r$ in the region where the residual droplet is present. Figure 17a shows residual droplet volume vs. ΔP , where the open blue circles are for droplets formed behind the defect, and the open red triangles are for droplets formed in front of the defect. It can be seen that the volume of the droplet formed behind the defect decreases with ΔP . This result can be rationalized by examining the droplet profiles when the receding contact line approaches the defect. Figure 17b shows these droplet profiles for different ΔP values. For each case, the receding contact line slows down as it approaches the defect. As ΔP increases, the depinned advancing contact line slides faster, leading to a more elongated droplet shape (figure 17b).

This results in a larger portion of the droplet being trapped behind the defect just before the residual droplet is pinched-off. Thus, a larger residual droplet is formed behind the defect for a larger ΔP value.

Figure 17a also shows that the volume of the residual droplet in front of the defect decreases with ΔP . This can be rationalized by noting that because the receding contact line slides faster after depinning from the defect for larger ΔP values, there is a shorter time for droplet pinch-off and a smaller residual droplet is formed in front of the defect.

8 Conclusions

We have developed a lubrication-theory-based model to study droplet depinning on rough substrates due to the flow of a surrounding fluid caused by an imposed pressure gradient. In contrast to commonly used force-balance models, ^{9,10,12} our model allows for the calculation of steady and transient droplet shapes. In addition, we explicitly account for surface roughness by considering the presence of topographical defects, an important feature not considered in prior computational studies. ^{20–25} Another significant difference from prior work is that our model requires specification of only an equilibrium contact angle via a disjoining-pressure function, with advancing and receding contact angle values being outputs of (rather than inputs to) our calculations that are determined by surface topography. Simple analytical models are able to account for many of the features observed in the numerical simulations. A key advantage of the lubrication-theory-based model we have developed is that it can readily be extended to study more complicated situations involving chemical heterogeneity (via a spatially varying disjoining pressure^{28,29}) and three-dimensional effects.

Below a critical value of the pressure gradient, ΔP_{crit} , the advancing and the receding contact lines of the droplet remain pinned at the defects. Above ΔP_{crit} , the shear force acting on the droplet due to the flow of the surrounding fluid exceeds the surface-tension force acting along the contact line, leading to droplet depinning. The pinning-depinning transition can also be understood in terms of a balance between capillary-pressure gradients and disjoining-pressure gradients. Our simulations reveal that the receding and advancing contact lines always pin at the points on the defects that have the maximum negative slope because this maximizes the surface-tension force acting on the droplet. This is a potentially important finding for applications such as inkjet printing and spray coating, where substrate topography could be designed to pin droplets at specific locations to obtain desired patterns.

As the viscosity of the surrounding fluid increases, ΔP_{crit} reaches a minimum before increasing due to a reduction in the shear force acting on the droplet. The presence of this minimum could be exploited to make processes such as oil recovery and crossflow microemulsification more efficient. Consistent with experimental observations, ¹² our model predicts that larger droplet volumes require a lower ΔP_{crit} , again due to the way the shear force behaves. Less wettable substrates increase the values of ΔP_{crit} due to the change in surface-tension forces, which are influenced both by the equilibrium contact angle and the maximum slope of the substrate topography, γ_{max} . This behavior is also consistent with experimental observations.⁹ Finally, it is also found that residual droplets may be formed behind and in front of the defect after the droplet depins if $\gamma_{max} > \theta_{rcl}$, which has implications for the efficiency of applications such as oil recovery, surface cleaning, and microemulsification.

Although we have considered Gaussian-shaped defects, we expect that our findings will generalize to other defect shapes for situations consistent with the lubrication approximation. Our results also serve as motivation for numerical simulations that relax the lubrication approximation, which are needed to address situations such as (i) defects with vertical sides (e.g., cylindrical and rectangular posts³⁸) or (ii) droplet-fluid interfaces that become vertical due to sufficiently large contact angles or forces that produce "lift-off" of the droplet from the substrate. We expect that some of our findings will generalize to three-dimensional defects as well, as long as the lateral length scale of the defects is sufficiently large compared to the other length scales characterizing the flow geometry. Three-dimensional effects can be addressed within the lubrication approximation, and our work motivates and can be used to help validate such calculations.

Acknowledgments

This material is based upon work supported by the National Science Foundation under Grant No. CBET-1935968. We thank C. Larsson for helpful discussions.

Declaration of interests

The authors report no conflicts of interest.

Appendix

In this section, we derive the expression for the force balance used in §4.2. We assume that the droplet has a dimensional width L'_z along the z-direction (not shown in figure 1a). The dimensional shear force can be estimated as $F_s' \sim L_z' \int_s \mathbf{n} \cdot \mathbf{T}' \cdot \mathbf{t} \, ds'$, where the primes represent dimensional quantities.

The dimensional surface-tension force is estimated by assuming a circular contact line of dimensional diameter D', such that the contact angle in the entire advancing half is θ_{acl} , and the contact angle in the entire receding half is θ_{rcl} :¹²

$$F'_{cl} = D' \int_0^{\pi/2} \sigma \cos \theta_{acl} \cos \alpha \, d\alpha + D' \int_{\pi/2}^{\pi} \sigma \cos \theta_{rcl} \cos \alpha \, d\alpha , \qquad (A.1)$$

$$F'_{cl} = D'\sigma(\cos\theta_{rcl} - \cos\theta_{acl}), \tag{A.2}$$

where $\alpha \in [0, \pi]$ (due to symmetry) denotes the angular position along the contact line such that $\alpha \in [0, \pi/2]$ spans the advancing half of the droplet, and $\alpha \in [\pi/2, \pi]$ spans the receding half of the droplet. The dimensional force balance is represented as:

$$(D'\sigma)(\cos\theta_{rcl} - \cos\theta_{acl}) \sim L'_z \int_s \mathbf{n} \cdot \mathbf{T}' \cdot \mathbf{t} \, ds',$$
 (A.3)

We non-dimensionalize the stresses using a capillary pressure $\sigma W'/L^2$, and assume $W' \sim h'_{max}$ and $L' \sim D'$, where primes have been used on W and L for notational consistency. This yields:

$$(D^2/h_{max})(L'^2/W'L'_z)(\cos\theta_{rcl} - \cos\theta_{acl}) \sim \int_s \mathbf{n} \cdot \mathbf{T} \cdot \mathbf{t} \, ds, \tag{A.4}$$

where D = D'/L' is the dimensionless droplet diameter, $h_{max} = h'_{max}/W'$ is the dimensionless maximum droplet height, and **T** is the dimensionless droplet stress tensor. Assuming that $L'^2/(W'L'_z) \sim 1$, which implies that $L'_z \sim L'/\epsilon$, where $\epsilon = W'/L'$, yields the dimensionless force balance:

$$(D^2/h_{max})(\cos\theta_{rcl} - \cos\theta_{acl}) \sim \int_{s} \mathbf{n} \cdot \mathbf{T} \cdot \mathbf{t} \, ds.$$
 (A.5)

References

- [1] C Charcosset, I Limayem, and H Fessi. The membrane emulsification process—a review. Journal of Chemical Technology & Biotechnology: International Research in Process, Environmental & Clean Technology, 79(3):209–218, 2004.
- [2] A Salama. On the estimation of the size of a droplet emerging from a pore opening into a crossflow field. *Soft Matter*, 18(9):1920–1940, 2022.
- [3] J Chatterjee. A criterion for buoyancy induced drop detachment based on an analytical approximation of the drop shape. *Colloids and Surfaces A: Physicochemical and Engineering Aspects*, 178(1-3):249–263, 2001.
- [4] DM Eckmann, DP Cavanagh, and AB Branger. Wetting characteristics of aqueous surfactant-laden drops. *Journal of Colloid and Interface Science*, 242(2):386–394, 2001.
- [5] H Lu, Q Yang, X Xu, and HL Wang. Effect of the mixed oleophilic fibrous coalescer geometry and the operating conditions on oily wastewater separation. *Chemical Engineering & Technology*, 39(2):255–262, 2016.
- [6] JR Landel and DI Wilson. The fluid mechanics of cleaning and decontamination of surfaces.

 Annual Review of Fluid Mechanics, 53:147–171, 2021.
- [7] AK Gupta and S Basu. Deformation of an oil droplet on a solid substrate in simple shear flow. *Chemical Engineering Science*, 63(22):5496–5502, 2008.
- [8] GK Seevaratnam, H Ding, O Michel, JYY Heng, and OK Matar. Laminar flow deformation of a droplet adhering to a wall in a channel. *Chemical Engineering Science*, 65(16):4523–4534, 2010.
- [9] S Madani and A Amirfazli. Oil drop shedding from solid substrates by a shearing liquid. Colloids and Surfaces A: Physicochemical and Engineering Aspects, 441:796–806, 2014.
- [10] H Lu, X Xu, LS Xie, HL Wang, GN Sun, and Q Yang. Deformation and crawling of oil drop on solid substrates by shearing liquid. Chemical Engineering Science, 195:720–729, 2019.

- [11] AJB Milne and A Amirfazli. Drop shedding by shear flow for hydrophilic to superhydrophobic surfaces. *Langmuir*, 25(24):14155–14164, 2009.
- [12] J Fan, MCT Wilson, and N Kapur. Displacement of liquid droplets on a surface by a shearing air flow. *Journal of Colloid and Interface Science*, 356(1):286–292, 2011.
- [13] IV Roisman, A Criscione, C Tropea, DK Mandal, and A Amirfazli. Dislodging a sessile drop by a high-Reynolds-number shear flow at subfreezing temperatures. *Physical Review* E, 92(2):023007, 2015.
- [14] K Sugiyama and M Sbragaglia. Linear shear flow past a hemispherical droplet adhering to a solid surface. *Journal of Engineering Mathematics*, 62:35–50, 2008.
- [15] CW Extrand and Y Kumagai. Liquid drops on an inclined plane: The relation between contact angles, drop shape, and retentive force. *Journal of Colloid and Interface Science*, 170(2):515–521, 1995.
- [16] AI ElSherbini and AM Jacobi. Retention forces and contact angles for critical liquid drops on non-horizontal surfaces. *Journal of Colloid and Interface Science*, 299(2):841–849, 2006.
- [17] M Bouteau, S Cantin, F Benhabib, and F Perrot. Sliding behavior of liquid droplets on tilted Langmuir-Blodgett surfaces. *Journal of Colloid and Interface Science*, 317(1):247– 254, 2008.
- [18] RTP Chow and EB Dussan. On the ability of drops or bubbles to stick to non-horizontal surfaces of solids. *Journal of Fluid Mechanics*, 137:1–29, 1983.
- [19] C Antonini, FJ Carmona, E Pierce, M Marengo, and A Amirfazli. General methodology for evaluating the adhesion force of drops and bubbles on solid surfaces. *Langmuir*, 25(11):6143–6154, 2009.
- [20] X Li and C Pozrikidis. Shear flow over a liquid drop adhering to a solid surface. *Journal of Fluid Mechanics*, 307:167–190, 1996.
- [21] P Dimitrakopoulos and JJL Higdon. On the displacement of three-dimensional fluid droplets from solid surfaces in low-Reynolds-number shear flows. *Journal of Fluid Mechanics*, 377:189–222, 1998.

- [22] P Dimitrakopoulos and JJL Higdon. On the displacement of three-dimensional fluid droplets adhering to a plane wall in viscous pressure-driven flows. *Journal of Fluid Mechanics*, 435:327–350, 2001.
- [23] AD Schleizer and RT Bonnecaze. Displacement of a two-dimensional immiscible droplet adhering to a wall in shear and pressure-driven flows. *Journal of Fluid Mechanics*, 383:29–54, 1999.
- [24] H Ding and PDM Spelt. Onset of motion of a three-dimensional droplet on a wall in shear flow at moderate Reynolds numbers. *Journal of Fluid Mechanics*, 599:341–362, 2008.
- [25] H Ding, MNH Gilani, and PDM Spelt. Sliding, pinch-off and detachment of a droplet on a wall in shear flow. *Journal of Fluid Mechanics*, 644:217–244, 2010.
- [26] D Deng, H Dong, Y Liang, and Z Zhao. Modeling the deformation and breakup of a surfactant-coated droplet on a roughness solid surface in shear flow. AIP Advances, 12(6):065313, 2022.
- [27] C Zhou and S Kumar. Two-dimensional two-layer channel flow near a step. *Chemical Engineering Science*, 81:38–45, 2012.
- [28] LW Schwartz and RR Eley. Simulation of droplet motion on low-energy and heterogeneous surfaces. *Journal of Colloid and Interface Science*, 202(1):173–188, 1998.
- [29] LW Schwartz. Hysteretic effects in droplet motions on heterogeneous substrates: Direct numerical simulation. *Langmuir*, 14(12):3440–3453, 1998.
- [30] L Espín and S Kumar. Droplet spreading and absorption on rough, permeable substrates. Journal of Fluid Mechanics, 784:465–486, 2015.
- [31] L Espín and S Kumar. Droplet wetting transitions on inclined substrates in the presence of external shear and substrate permeability. *Physical Review Fluids*, 2(1):014004, 2017.
- [32] V Charitatos, T Pham, and S Kumar. Droplet evaporation on inclined substrates. *Physical Review Fluids*, 6(8):084001, 2021.

- [33] N Savva and S Kalliadasis. Dynamics of moving contact lines: A comparison between slip and precursor film models. *Europhysics Letters*, 94(6):64004, 2011.
- [34] SK Kalpathy, LF Francis, and S Kumar. Thin-film models of liquid displacement on chemically patterned surfaces for lithographic printing processes. *Journal of Colloid and Interface Science*, 383(1):155–166, 2012.
- [35] J Park and S Kumar. Droplet sliding on an inclined substrate with a topographical defect. Langmuir, 33(29):7352–7363, 2017.
- [36] LH Tanner. The spreading of silicone oil drops on horizontal surfaces. *Journal of Physics D: Applied Physics*, 12(9):1473, 1979.
- [37] M Mortazavi and SY Jung. Role of droplet dynamics on contact line depinning in shearing gas flow. *Langmuir*, 2023.
- [38] A Saal, BB Straub, HJ Butt, and R Berger. Pinning forces of sliding drops at defects. Europhysics Letters, 139(4):47001, 2022.